Electrocatalysis

Correlation between Precursor Properties and Performance in the Oxygen Reduction Reaction of Pt and Co “Core-shell” Carbon Nitride-based Electrocatalysts

--Manuscript Draft--

Manuscript Number:	
Full Title:	Correlation between Precursor Properties and Performance in the Oxygen Reduction Reaction of Pt and Co “Core-shell” Carbon Nitride-based Electrocatalysts
Article Type:	SI: Electrocat 2018
Order of Authors:	Vito Di Noto, Ph.D.
	Enrico Negro, Ph.D.
	Angeloclaudio Nale, Ph.D.
	Pawel J. Kulesza, Ph.D.
	Iwona A. Rutkowska, Ph.D.
	Keti Vezzù, Ph.D.
	Gioele Pagot, Ph.D.
Corresponding Author:	Vito Di Noto, Ph.D. Università degli Studi di Padova Padova, Veneto ITALY
Corresponding Author Secondary Information:	
Corresponding Author's Institution:	Università degli Studi di Padova
Corresponding Author's Secondary Institution:	
First Author:	Vito Di Noto, Ph.D.
First Author Secondary Information:	
Keywords:	PtCox carbon nitride based electrocatalysts; "Core-shell" morphology; Oxygen reduction reaction; CV-TF-RRDE method; PEMFC fabrication and testing.
Order of Authors Secondary Information:	
Suggested Reviewers:	Lior Elbaz Bar-Ilan University lior.elbaz@biu.ac.il
	Nicolas Alonso-Vante Universite de Poitiers nicolas.alonso.vante@univ-poitiers.fr
	Peter Pintauro Vanderbilt University pn.pintauro@vanderbilt.edu
	Andrew Herring Colorado School of Mines aherring@mines.edu
	Plamen Atanassov University of California Irvine plamen@unm.edu
Funding Information:	Horizon 2020 Framework Programme (Graphene Core 2 785219) — Not applicable
	Università degli Studi di Padova (BIRD187913) — Not applicable

	Università degli Studi di Padova (Hierarchical electrocatalysts with a low platinum loading for low-temperature fuel cells – HELPER)	Not applicable
	Narodowym Centrum Nauki (2018/29/B/ST5/02627)	Prof. Pawel J. Kulesza

Abstract:	This report shows the synthesis of a new family of “core-shell” carbon nitride (CN)-based electrocatalysts (ECs) for the oxygen reduction reaction (ORR) in acid medium. The ECs comprise “cores” of carbon black nanoparticles (NPs), that are covered by a CN “shell” embedding the active sites. The latter include Pt as the “active metal” and Co as the “co-catalyst”. The interplay between the synthesis parameters, the chemical composition and the ORR performance of the final ECs is elucidated. In particular, the ORR performance and reaction mechanism are studied both in an: (i) “ex-situ” setup, by means of cyclic voltammetry with thin-film rotating ring-disk electrode (CV-TF-RRDE) measurements; and (ii) “in-situ” experiment, i.e., in single proton exchange membrane fuel cells (PEMFCs) tested under operating conditions. A structural hypothesis is proposed, that explains both the “ex situ” and the “in situ” ORR results on the basis of: (i) the relative amounts of the reactants used in the precursor synthesis; and (ii) the main temperature of the pyrolysis process (Tf) adopted in the preparation of the ECs. It is shown that the understanding of the fundamental features of the physicochemical processes involved in the preparation of the ECs is crucial in order to improve the proposed synthesis route and to yield ORR ECs exhibiting a performance level beyond the state of the art.

UNIVERSITÀ DEGLI STUDI DI PADOVA

DIPARTIMENTO DI INGEGNERIA INDUSTRIALE

Prof. Vito Di Noto
via F. Marzolo, 9
35131 Padova

tel. +39 049 8275229
fax +39 049 8275229
vito.dinoto@unipd.it
www.dii.unipd.it

CF 80006480281
P.IVA 00742430283

Sede amministrativa
via Gradenigo 6/a
35131 Padova

Sede M:
via Marzolo, 9
35131 Padova

Sede V:
via Venezia, 1
35131 Padova

Prof. Gregory Jerkiewicz
Editor-in-Chief, Electrocatalysis (Springer)
Department of Chemistry,
Queen's University, Kingston, ON, Canada

Padova, 8 August 2019

Submission of manuscript for consideration in the Special Issue of the journal *"Electrocatalysis"* dedicated to the *"Electrocatalysis 2018"* conference

Dear Prof. Gregory Jerkiewicz,

On behalf of my co-authors and myself, I would like to submit the attached manuscript, entitled '*Correlation between Precursor Properties and Performance in the Oxygen Reduction Reaction of Pt and Co "Core-shell" Carbon Nitride-based Electrocatalysts*' by Vito Di Noto, Enrico Negro, Angeloclaudio Nale, Pawel J. Kulesza, Iwona A. Rutkowska, Keti Vezzù, and Gioele Pagot as an Article in the Special Issue of the journal *"Electrocatalysis"* (P. J. Kulesza and I. A. Rutkowska, Guest Editors) dedicated to the *"Electrocatalysis 2018"* conference.

This report describes the synthesis of a new family of *"core-shell"* carbon nitride (CN)-based electrocatalysts (ECs) for the oxygen reduction reaction (ORR). The ECs comprise *"cores"* of carbon black nanoparticles (NPs), that are covered by a CN *"shell"* embedding the active sites. The latter include Pt as the *"active metal"* and Co as the *"co-catalyst"*. The interplay between the synthetic parameters, the chemical composition and the ORR performance of the final ECs is elucidated. In particular, the ORR performance and reaction mechanism are studied both: (i) in an *"ex-situ"* setup, by means of cyclic voltammetry with thin-film rotating ring-disk electrode (CV-TF-RRDE) measurements; and (ii) *"in-situ"*, *i.e.,* in single proton exchange membrane fuel cells (PEMFCs) tested under operating conditions. A structural hypothesis is proposed, that rationalizes the experimental ORR results obtained both *"ex-situ"* and *"in-situ"* on the basis of: (i) the relative amounts of the reactants used in the synthesis; and (ii) the temperature of the final step of the pyrolysis process adopted in the preparation of the ECs. It is shown that, once the fundamental mechanisms that modulate the interplay between the synthetic parameters, the physicochemical properties

and the electrochemical performance of the ECs is understood, the proposed synthetic route can be rationally tailored to yield ORR ECs exhibiting a performance level beyond the state of the art.

This manuscript is interdisciplinary and will require reviewers that are knowledgeable in ORR electrochemistry, RRDE measurements, fabrication and testing of PEMFCs. We therefore take the liberty to propose the following reviewers:

- Lior Elbaz (Bar-Ilan University, Israel), E-mail address: lior.elbaz@biu.ac.il
- Nicolas Alonso-Vante (University of Poitiers, France), E-mail address: nicolas.alonso.vante@univ-poitiers.fr
- Peter Pintauro (Vanderbilt University, USA), E-mail address: pn.pintauro@vanderbilt.edu
- Andrew Herring (Colorado School of Mines, USA), E-mail address: aherring@mines.edu
- Plamen Atanassov (University of California, Irvine, USA), E-mail address: plamen@unm.edu

This manuscript is not under consideration for publication in other journals and has not been published elsewhere in any other format.

We thank you for your consideration and look forward to hearing from you.

Sincerely,
Vito Di Noto

Correlation between Precursor Properties and Performance in the Oxygen Reduction Reaction of Pt and Co *"Core-shell"* Carbon Nitride-based Electrocatalysts

Vito Di Noto[1,2*], Enrico Negro[1,3], Angeloclaudio Nale[1], Pawel J. Kulesza[4], Iwona A. Rutkowska[4], Keti Vezzù[1,2], Gioele Pagot[1,3].

[1] Section of Chemistry for the Technology (ChemTech), Department of Industrial Engineering, University of Padova, Via Marzolo 9, I-35131 Padova (PD), Italy.

[2] Consorzio Interuniversitario Nazionale per la Scienza e Tecnologia dei Materiali - INSTM, Via Marzolo 1, I-35131 Padova (PD), Italy

[3] Centro Studi di Economia e Tecnica dell'Energia *"Giorgio Levi Cases"*, Via Marzolo 9, I-35131 Padova (PD), Italy.

[4] Faculty of Chemistry, University of Warsaw, Pasteura 1, PL-02-093 Warsaw, Poland

*Corresponding Author. E-mail address: vito.dinoto@unipd.it

Abstract

This report shows the synthesis of a new family of *"core-shell"* carbon nitride (CN)-based electrocatalysts (ECs) for the oxygen reduction reaction (ORR) in acid medium. The ECs comprise *"cores"* of carbon black nanoparticles (NPs), that are covered by a CN *"shell"* embedding the active sites. The latter include Pt as the *"active metal"* and Co as the *"co-catalyst"*. The interplay between the synthesis parameters, the chemical composition and the ORR performance of the final ECs is elucidated. In particular, the ORR performance and reaction mechanism are studied both in an: (i) *"ex-situ"* setup, by means of cyclic voltammetry with thin-film rotating ring-disk electrode (CV-TF-RRDE) measurements; and (ii) *"in-situ"* experiment, *i.e.*, in single proton exchange membrane fuel cells (PEMFCs) tested under operating conditions. A structural hypothesis is proposed, that explains both the *"ex situ"* and the *"in situ"* ORR results on the basis of: (i) the relative amounts of the reactants used in the precursor synthesis; and (ii) the main temperature of the pyrolysis process (T_f) adopted in the preparation of the ECs. It is shown that the understanding of the fundamental features of the physicochemical processes involved in the preparation of the ECs is crucial in order to improve the proposed synthesis route and to yield ORR ECs exhibiting a performance level beyond the state of the art.

Keywords: $PtCo_x$ carbon nitride based electrocatalysts; *"Core-shell"* morphology; Oxygen reduction reaction; CV-TF-RRDE method; PEMFC fabrication and testing.

1. Introduction

The oxygen reduction reaction (ORR) is an electrochemical process that is of very high fundamental interest and of immense utility for several practical applications [1]. Indeed, the ORR is involved in the operation of several families of advanced electrochemical energy conversion and storage (EECS) devices such as fuel cells (FCs) and metal-air batteries [2, 3]. These devices are currently under intense research for their potential role in the modern restructuring of the energy systems at the global level [4-6], with the ultimate purpose to minimize the consumption of fossil fuels and utilize on a large scale the energy obtained from renewable sources [7]. In particular, the slow kinetics of the ORR is one of the most relevant fundamental hurdles that curtails the energy conversion efficiency of FCs [1, 8]. This shortcoming is particularly serious for fuel cells operating at low temperatures such as proton-exchange membrane fuel cells (PEMFCs) fuelled with hydrogen [8]. These systems are particularly promising for practical applications (*e.g.*, auxiliary power units and light-duty vehicles) owing to their very high power density and simple construction [8, 9].

In a PEMFC the ORR takes place in extremely harsh conditions in terms of both very low pH values (owing to the acidic character of the electrolyte) and high electrochemical potentials (that are necessary to maximize the energy conversion efficiency of the device) [10, 11]. Furthermore, PEMFCs yield very large current densities, on the order of several hundreds of $mA \cdot cm^{-2}$ of electrode area or more [12, 13], that are necessary to achieve a power density compatible with the applications [14]. In order to satisfy such demanding needs, the ORR must be promoted by suitable electrocatalysts (ECs) [15]. The latter must also be highly stable, to warrant a high durability [16]. The traditional approach to comply with all these specifications is to design nanocomposite ECs comprising nanostructured carbons that support platinum nanoparticles with a large surface area [3]. The resulting ECs exhibit an acceptable performance; however, the high loading of platinum and the poor durability are still major roadblocks that inhibit the large-scale rollout of PEMFCs [17].

Several approaches are pursued to develop ORR ECs able to address the shortcomings of state-of-the-art ECs. One possibility is to raise the performance of the Pt active sites by developing ECs comprising multi-metal alloy NPs, that are typically based on Pt and one or more transition metals such as Ni [18]and Co [3]. A massive amount of research is also currently devoted to develop *"Pt-free"* ECs [19, 20]. Important progresses have been made recently, but the performance and durability of these ECs are still insufficient for implementation in PEMFCs able to match the requirements set by applications [21]. Other avenues of research aim at developing exotic nanostructures such as octahedra or hollow Pt-based nanocages, that promise a truly outstanding performance [22-24]. However, several of these ECs have not been tested in a PEMFC, hindering the appraisal of their real potential to satisfy practical applications [25]. Finally, very often the synthetic protocols adopted to obtain the advanced ORR ECs mentioned above are able to yield only very small amounts of product and are difficult to upscale. This is a further obstacle towards industrialization [24].

The ECs reported here are obtained by means of a unique and extremely flexible preparation protocol, whose development started more than 20 years ago in our laboratory [26-28]. The here customized preparation protocol: (i) is able to yield easily consistent amounts of products, on the order of grams [27]; and (ii) allows for the accurate modulation of the chemical composition and the morphology of the products, giving rise to high-performance carbon nitride (CN)-based ECs for the ORR [26]. In these ECs, most of the ORR performance is provided by an *"active metal"* [26], typically Pt [29], Pd [30] or Fe [31]. Another element is introduced as a *"co-catalyst"*, further reducing the ORR overpotential [26]. In particular, the materials described in this report are classified as *"second-generation"* CN-based ECs as they exhibit a *"core-shell"* morphology [32]. The *"cores"* consist of carbon nanoparticles with a good electrical conductivity, that are covered by a CN *"shell"* including less than 5 wt% of N to minimize ohmic drops. Indeed, the latter compromise the overall performance of the PEMFC mounting the CN-based EC [26]. The *"shell"*

of the ECs presented here embeds $PtCo_x$ nanoparticles (NPs), that are stabilized in *"coordination nests"* based on C- and N- ligands [31, 32] meant to raise the durability of the material. The active sites for the ORR are found on such $PtCo_x$ NPs, similarly to other *"second-generation"* CN-based ECs [33]. Hence, in the ECs described in this report Pt is the *"active metal"* and Co is the *"co-catalyst"*. The preparation protocol yielding the here reported ECs consists in the following main steps: (i) synthesis of a hybrid inorganic-organic precursor; (ii) multi-step pyrolysis processes; and (iii) a series of *"post-synthesis"* activation steps. It is found that the chemical composition and the structure of the hybrid inorganic-organic precursor play a crucial role to determine the physicochemical properties of the final EC and, consequently, its performance in the ORR both in *"ex-situ"* measurements by cyclic voltammetry with thin-film rotating ring-disk electrode (CV-TF-RRDE) and in single PEMFC [33, 34]. This report is part of a series of systematic fundamental studies meant to clarify the interplay between [33-35]: (i) the chemical features and the stoichiometry of the reactants; (ii) the reaction mechanisms involved in the formation of the hybrid inorganic-organic precursor; (iii) the structure of the precursor; (iv) the details of the multi-step pyrolysis process; (v) the physicochemical properties of the final ECs; and finally (vi) the ORR reaction pathway and ORR performance, both in *"ex-situ"* and in single PEMFC studies. In particular, the aim of this report is the study of new ECs: (i) based on Co as the metal *"co-catalyst"*; (ii) to investigate the effects on the ORR performance of the amount of binder used in the synthesis of the nZ-IOPE precursor and of the temperature (T_f) of the main pyrolysis step.

2. Experimental

2.1. Reagents

Potassium tetrachloroplatinate (II) 98%, (K_2PtCl_4) and H_2SO_4 95-97% are purchased from Sigma-Aldrich. H_2O_2 36% vol., is supplied by ABCR GMBH. Potassium hexacyanocobaltate (III) 95%, ($K_3Co(CN)_6$), is supplied by Fluka. D(+)-sucrose, biochemical grade, is Acros reagent. $HClO_4$ 70% is obtained from Fluka. All the reagents are used as received. XC-72R carbon black is provided as a courtesy by Carbocrom s.r.l., and is washed with H_2O_2 10% vol. prior to use. The commercial EC-20 product (ElectroChem Inc.) with a nominal Pt loading of 20 wt% is used as a reference electrocatalyst and does not undergo any further purification and washing procedure.

2.2. Synthesis of the electrocatalysts

The synthesis of the ECs reported in this work is carried out in accordance with a protocol described in the scientific and technical literature [27, 33]. Briefly, 133.4 mg of sucrose are dissolved into the minimum amount of water (≈ 1 mL), yielding a clear viscous solution. A second deep red solution is obtained by dissolving 400 mg of K_2PtCl_4 into the minimum amount of water (≈ 1 mL). The viscous sucrose solution is added dropwise, under vigorous stirring, into the deep red solution including K_2PtCl_4. 533.5 mg of XC-72R are further added; the product is extensively homogenized by stirring and ultrasonication, yielding a homogeneous black dispersion. A second dispersion is prepared following exactly the same protocol; the only difference is that 332.4 mg of $K_3Co(CN)_6$ are used instead of K_2PtCl_4. The dispersion comprising K_2PtCl_4 is added dropwise, under vigorous stirring, to the dispersion including $K_3Co(CN)_6$. The product is extensively homogenized by sonication, stirred for 24 h and left to rest for additional 48 h; afterwards, it is treated overnight at 120 °C in an oven in order to remove most of the water. The resulting black solid is transferred into a quartz tube, where it undergoes the following two-step thermal treatment: (i) 150 °C for 7 h; (ii) 300 °C for 2 h. The entire treatment is carried out under a dynamic vacuum of

10^{-1} mbar. A general label indicating all the materials presented in this report is *"PtCo-CN$_l$ T$_f$/C$_w$"*, where *"**w**"* is the mass ratio between the sucrose binder and XC-72R NPs of the *"core"* used in the preparation of the precursor. One aliquot of EC is brought back into a quartz tube, where it undergoes an additional pyrolysis step at T_f = 500 °C, that lasts for two hours under a dynamic vacuum of 10^{-1} mbar. The product is then: (i) washed three times with water; (ii) treated with H_2O_2, 10% vol.; and (iii) dried overnight in an oven at T = 120 °C. Three additional ECs are obtained at different T_f: (i) T_f = 600 °C yields *"PtCo-CN$_l$ 600/C$_{1/4}$"*; (ii) T_f = 700 °C yields *"PtCo-CN$_l$ 700/C$_{1/4}$"*; and (iii) T_f = 900 °C yields *"PtCo-CN$_l$ 900/C$_{1/4}$"*. Two additional ECs are synthesized, that are exactly identical to that with **w** = 1/4, only changing the amount of sucrose: (i) 266.8 mg, resulting in the EC with **w** = 2/4; and (ii) 533.5 mg, yielding the EC with **w** = 4/4.

2.3. Intstruments and Methods

The wt% of K, Pt and Co is evaluated by means of Inductively-Coupled Plasma Atomic Emission Spectroscopy (ICP-AES) utilizing a SPECTRO Acros spectrometer with EndOnPlasma torch. The digestion of the samples is carried out as elsewhere reported [29] with an initial oxidation step executed at 650 °C for two hours. The emission lines are: λ (K) = 766.490 nm; λ (Pt) = 214.423 nm; λ (Co) = 228.616 nm. The assay of C, H, and N in the PtCo-CN$_l$ T$_f$/C$_w$ ECs is measured by microanalysis using a FISONS EA-1108 CHNS-O instrumentation. High-resolution thermogravimentric measurements are carried out with a High-Res modulated TGA 2950 thermogravimetric analyzer using an open platinum pan and a temperature range from 30 to 900°C. The measurements are collected under an air oxidizing atmosphere. The morphology is elucidated by means of a high-resolution transmission electron microscopy (HR-TEM) analysis, that is executed with a JEOL 3010 instrumentation operating at 300 kV. The system is equipped with a Gatan slowscan 794 CCD camera. The samples are dispersed in isopropyl alcohol using a probe

sonicator; a 5 μL drop of the suspension is dried on a holey carbon film supported on a 3 mm copper grid.

2.4. Electrochemical Measurements

Electrochemical measurements with the CV-TF-RRDE method are performed according to the procedure reported elsewhere [31, 35]. Briefly, each EC is mixed with XC-72R in a 1:1 weight ratio and ground in a mortar, attaining a homogeneous powder. Suitable amounts of milli-Q water and a commercial Nafion 1100 dispersion (Alfa Aesar, 5% weight) are used to suspend these mixtures, yielding an EC ink. The label *"Pt/C reference"* corresponds to the EC-20 electrocatalyst (ElectroChem, 20 wt% Pt on XC-72R). This EC is processed with a similar procedure, but without the addition of further XC-72R; it is tested as a benchmark to the ECs presented in this report. Each electrode has the same platinum loading on the tip, corresponding to 12 $\mu g \cdot cm^{-2}$. The setup used to carry out the electrochemical measurements consists of a Model 636 Rotating Ring-Disk Electrode system (Princeton Applied Research) connected to a multi-channel VSP potentiostat/galvanostat (BioLogic). The exact determination of the RHE potential is carried out as described elsewhere before each measurement [36]. In a previous report we describe in detail the experimental setup and the measurement procedure used to execute the electrochemical investigations presented in this report for the determination of both the electrochemically-active surface area (ECSA) by CO_{ad} stripping and the performance in the ORR [37]. The only differences are that here the sweeps are executed at a scan rate equal to 20 $mV \cdot sec^{-1}$ and the electrochemical cell is thermostated at 25 °C.

2.5. Fabrication of membrane-electrode assembly and tests in single PEMFC

The membrane-electrode assemblies (MEAs) are prepared with a catalyst-coated substrate procedure as described elsewhere [33]. Some details are provided here for clarity's sake. Commercial Nafion117 membranes (Ion Power) are adopted as the membrane and GDS1120

carbon paper (Ballard Material Products) is used as the support for electrocatalytic layers. The membranes are cleaned by means of the following three-step procedure: (i) immersion in 3 wt% H_2O_2 for 1 h; (ii) immersion in 1 M H_2SO_4 for 1 h; (iii) treatment in doubly distilled water for 1 h. (i)-(iii) are carried out at 80 °C. The anode electrocatalyst is EC-20, with a platinum loading of 0.4 $mg \cdot cm^{-2}$. The cathode electrocatalysts are dispersed with XC-72R in a 1:1 weight ratio. In each MEA, the cathode electrocatalytic layer includes a platinum loading of 0.1 $mg \cdot cm^{-2}$ and an overall Nafion/C mass ratio equal to 0.6. Hot-pressing is used to fuse the resulting gas diffusion electrodes (GDEs) onto the membranes, as previously described [33]. A back pressure (BP) of the reagents equal to either 4 and 1 bar is used during single fuel cell tests performed as described elsewhere [33].

3. Results and Discussion

3.1. The nanocomposite zeolitic inorganic-organic polymer electrolyte (nZ-IOPE) precursor

The precursors used for the preparation of the ECs here described belong to the family of *"nanocomposite zeolitic inorganic-organic polymer electrolytes"* (nZ-IOPE) [31]. Such precursors are obtained by bringing together in the same aqueous reaction mixture: (i) a coordination compound of a *"soft"* metal (*e.g.*, Pt) bearing good leaving groups (*e.g.*, chloride ligands) [29, 38]; (ii) a cyanometalate complex (*e.g.*, $Ni(CN)_4^{2-}$ [29, 33], $Fe(CN)_6^{4-}$ [35] or $Co(CN)_6^{3-}$ [30]) acting as an inorganic ligand; (iii) an organic binder including a large number of hydroxyl groups (*e.g.*, sucrose) to crosslink the inorganic metal complexes thus formed [29, 30, 33, 35, 39]; and finally (iv) a carbon support endowed with surface hydroxyl groups (*e.g.*, XC-72R nanoparticles) [33]. After mixing all the above-described components a complex series of equilibria are established in the dispersion that, by sol-gel and gel-plastic transitions [33, 40], lead to the formation of the final three-dimensional networked nZ-IOPE [33, 35, 40]. It should be observed that, in order to study the effect of the binder on the performance of the final ECs, the nZ-IOPE precursors here described are based on the same fixed amounts of of K_2PtCl_4, $K_3Co(CN)_6$ and XC-72R carbon black NPs. Thus, the only difference in the precursor samples is the amount of the sucrose binder, that in PtCo-CN_l T_f/C_w (500 °C < T_f < 900 °C) increases from **w** = 1/4 to **w** = 4/4. *"**w**"* is the mass ratio between the sucrose binder and the carbon black NPs.

The literature reports that in this type of systems not all the binder molecules introduced in the starting reaction mixture are actually incorporated into the backbone of the 3D hybrid inorganic-organic structure of the Z-IOPE precursor. Indeed, in the case of a Z-IOPE prepared starting from one mole of K_2PdCl_4, two moles of $K_3Co(CN)_6$ and seven moles of the PEG600 binder, it was found that only two moles of the binder are actually included in the 3D network backbone of the Z-IOPE where they are acting as bridges between the anionic metal complex clusters resulting from

the reaction of $PdCl_4^{2-}$ with the $Co(CN)_6^{3-}$ ligand [41]. The remaining five PEG600 moles form interstitial PEG600 domains embedded in the 3D hybrid plastic network [41]. In details, the presence of such cavities filled by ligand molecules within the hybrid inorganic-organic network was also revealed in similar systems based on Fe and Pd (or Sn) clusters bonded together by means of glycerol bridges. In this case the interstices of the 3D hybrid structure were flooded with glycerol molecules [40]. On the basis of such observations, and considering that sucrose is characterized by a molar ratio ρ = –OH/C equal to 0.6 (ρ for PEG600 and glycerol is $\approx$ 0.04 and 1, respectively), we expect that a part of the sucrose binder forms sucrose domains embedded in the structural interstices of the 3D hybrid inorganic-organic structure of the Z-IOPE precursor. The presence of these domains modulates the density of the 3D hybrid network per unit volume of the Z-IOPE material included in the nZ-IOPE precursor. During the pyrolysis process the 3D hybrid network gives rise to the $PtCo_x$ nanoparticles (NPs) [34] and its density is responsible of the size and the surface area of the final $PtCo_x$ NPs (see Table 2) [42]. An excess of sucrose, which in the precursor forms large sucrose domains: (i) significantly modifies the EC matrix during the pyrolysis process, giving so rise to the disruption of the continuous and compact CN *"shell"* embedding the $PtCo_x$ NPs; and (ii) increases the density of C inside the CN matrix, hindering the accessibility of reagents towards the active sites of the $PtCo_x$ NPs. To clarify these phenomena, in this report the aim is to study the effect of **w** on ORR performance and to evaluate the optimal **w** value to maximize the performance of the ECs.

3.2. Chemical composition of ECs

The chemical composition of the ECs in the bulk is evaluated by inductively-coupled plasma atomic emission spectroscopy (ICP-AES) and elemental analysis. Results are reported in Table 1. The ECs show practically constant Pt/Co molar ratios, with values of *ca.* 1. This result confirms that the proposed synthesis route is very feasible to control the metal stoichiometry of the ECs independently on T_f and starting reagent compositions. No evidence of metal losses is detected,

suggesting that the $PtCl_4^{2-}$ and the $Co(CN)_6^{3-}$ complexes are completely incorporated into the nZ-IOPE precursor. Indeed the obtained ECs include, in first approximation, the same wt% of Pt and Co. This observation is rationalized considering that during the final step of the pyrolysis most of the heteroatoms deriving from the sucrose reactant are removed as volatile species (*e.g.*, H_2O and CO_2) [33]. These processes eliminate part of the C provided by the sucrose to yield the total C remaining in the PtCo-CN_l T_f/C_w ECs. The concentration of H in the ECs is lower than 0.6 wt%, witnessing that the graphitization of the CN *"shell"* is practically complete [33], while N is equal to *ca.* 1 wt% or lower. This result demonstrates that N is successfully incorporated into the CN *"shell"*, allowing for the formation of a CN support matrix with a high electrical conductivity [26]. Finally it is noted that, among the PtCo-CN_l 600/C_w ECs, the N/Pt ratio is maximized at **w** = 2/4.

3.3. HR-TGA studies

Fig. 1 shows the HR-TGA profiles in oxidizing atmosphere of PtCo-CN_l T_f/C_w ECs, the Pt/C reference and the XC-72R carbon black (that is also used as the support in the Pt/C reference). In these profiles it is revealed that the thermal stability of PtCo-CN_l $T_f/C_{1/4}$ ECs increases on T_f, while that of PtCo-CN_l 600/C_w decreases as **w** is raised from 1/4 to 4/4. In general, PtCo-CN_l T_f/C_w ECs are more stable than the Pt/C reference. In the PtCo-CN_l 300/$C_{1/4}$ EC the main decomposition event takes place at *ca.* 40 °C above the Pt/C reference. Such difference increases to approximately 100 °C for PtCo-CN_l 500/$C_{1/4}$, PtCo-CN_l 600/$C_{1/4}$ and PtCo-CN_l 700/$C_{1/4}$, and reaches 120 °C for PtCo-CN_l 900/$C_{1/4}$. With respect to the Pt/C reference, the temperature of the main thermal degradation event of PtCo-CN_l 600/C_w ECs is *ca.* 70-100 °C higher.

These results suggest that the oxidation of the CN matrix is catalyzed at the interface between the $PtCo_x$ NPs and the CN *"shell"*. Indeed, Pt and Co active sites are very efficient to adsorb oxygen from the atmosphere and thus to catalyze the degradation of the matrix. The decomposition temperature of PtCo-CN_l $T_f/C_{1/4}$ ECs is thus correlated to the surface catalytic activity of the $PtCo_x$

NPs, that also depends on the ECSA (see Table 2) [42]. ECSA decreases on T_f and in general shows values that are smaller than those of the Pt/C reference. A smaller interfacial contact area between the $PtCo_x$ NPs and the support is thus expected. It is also noted that the pristine XC-72R carbon black undergoes oxidative decomposition at a much higher temperature in comparison with the Pt/C reference (over 630 °C *vs.* 400 °C, respectively). This evidence is easily ascribed to the absence of metal catalytic sites on the XC-72R carbon black. The lower decomposition temperature revealed for PtCo-CN_l 300/$C_{1/4}$ is attributed to the presence in this sample of a high density of small $PtCo_x$ NPs which result when metal diffusion phenomena in the matrix are hindered, inhibiting the coalescence of Pt and Co metal atoms into alloy NPs. The incomplete graphitization of the CN matrix at T_f = 300 °C produces a material with a high amount of oxygen, where the oxidation of the CN matrix at low temperatures is facilitated [35]. PtCo-CN_l 900/$C_{1/4}$ shows: (i) the smallest ECSA (see Table 2); and (ii) the lowest porosity (see Section 3.1), that is obtained from a precursor with a low amount of sucrose binder. Hence, the CN matrix of this EC, which is the most compact, inhibits the diffusion of oxygen at the interface [CN-matrix]/[$PtCo_x$ NPs] (see also Section 3.5.2). A shift to higher decomposition temperatures is attributed to the presence of nitrogen in the CN *"shell"* of the ECs (see Section 3.2). N is expected to stabilize the ECs by strengthening the interactions between the CN support and the $PtCo_x$ NPs [31, 43]. In PtCo-CN_l 600/C_w ECs, on **w** the pyrolysis of precursors provides CN matrices with an increasing quantity of highly defective C, which acts to lower the onset temperature of the thermal decomposition of these materials.

3.4. HR-TEM studies

The morphology of the PtCo-CN_l T_f/C_w ECs is very similar. Fig. 2 displays the morphology of PtCo-CN_l 600/$C_{2/4}$ as a representative example of all the ECs here proposed. Fig. 2(a) and Fig. 2(b) show the following main features of PtCo-CN_l 600/$C_{2/4}$: (i) black spots with a diameter of *ca.* 20 nm, that are homogeneously distributed in the CN *"shell"* and which correspond to the $PtCo_x$ NPs formed during the pyrolysis process; and (ii) a very rough support, consisting of spheroidal carbon black NPs with a diameter of *ca.* 30-50 nm (the *"core"*) wrapped by a CN *"shell"*. This *"core-shell"* morphology of ECs is shown in Fig. 2(c), where the *"shell"* appears as a rough, porous layer (thickness ≈ 5-10 nm) covering the carbon black NPs of the *"core"*. Finally, Fig. 2(d) and Fig. 2(d') allow to identify and analyze the composition of the dark spots of $PtCo_x$ NPs. In particular, the high-resolution micrograph displayed in Fig. 2(d) reveals a polycrystalline nanoparticle with an interplanar distance of *ca.* 2.2 nm. The latter corresponds to the spacing between the (111) planes of a $PtCo_x$ alloy that is isostructural with Pt and exhibits a similar cell constant. This information is consistent with the results obtained by WAXD and shown in Fig. ESI1.

3.5. Correlation between precursor stoichiometry and electrocatalyst performance

3.5.1. CV-TF-RRDE studies

The CO_{ad} stripping profiles of the ECs described in this report are displayed in Fig. 3. In CO_{ad} stripping experiments (see Fig. 3) the ECs reveal one main peak at E < 0.7 V *vs.* RHE. The CO_{ad} stripping peak of the Pt/C reference is detected at E ≈ 0.83 V *vs.* RHE. The Co atoms play a crucial role in the modulation of the electrochemical properties of the ECs, introducing in alloy NPs a significant surface strain due to the lattice mismatch phenomena (electronic effect) [44]. In this case, the stripping event of CO_{ad} is facilitated and shifts to lower potentials in comparison with the Pt/C reference [45]. The stripping of CO_{ad} is also facilitated by the presence of oxophilic Co oxide species on the NPs surface, that promote the oxidation of CO_{ads} (bifunctional effect) [46]. At **w** =

1/4 the support of the EC consists of carbon black NPs (the *"core"*) covered by a carbon nitride *"shell"* with a high content of C (a good reducing agent) [47]. In this case as T_f is raised the density of Co oxide species is progressively reduced by the CN matrix, decreasing the oxophilicity of the EC surface and the bifunctional effect above described, which facilitates the CO_{ad} stripping processes. As a result, on T_f in PtCo-CN_l $T_f/C_{1/4}$ ECs the CO_{ad} stripping peak progressively shifts to larger E values. The right panel of Fig. 3 shows that, with respect to PtCo-CN_l 600/$C_{1/4}$, the CO_{ad} stripping peak of both PtCo-CN_l 600/$C_{2/4}$ and PtCo-CN_l 600/$C_{4/4}$ is shifted to lower E values. This phenomenon is justified considering that during the pyrolysis process, the amount of heteroatoms (*e.g.*, H, O) provided in the CN matrix by sucrose increases on **w**. Consequently, with respect to **w** = 1/4, in samples with **w** = 2/4 and 4/4 a CN matrix with a lower reducing ability is expected. Hence, in this condition a larger fraction of oxophilic Co oxide species are present, which provide a stronger bifunctional effect that facilitates the stripping processes of CO_{ad}. The CV-TF-RRDE profiles of PtCo-CN_l $T_f/C_{w1/4}$ ECs are shown in Fig. 4.

Results indicate that at T_f < 900, the ORR overpotential of the PtCo-CN_l $T_f/C_{1/4}$ is similar to that of the Pt/C reference. In PtCo-CN_l 600/C_w samples the ORR overpotential decreases on **w**. The average number of electrons (n) that are exchanged during the ORR is evaluated through Equation (1)

$$n = \frac{4I_{ORR}}{I_{ORR}+\frac{I_r}{N}} \qquad (1)$$

where I_{ORR} is the current of the ORR process measured on the RRDE disk. I_{ORR} is determined by multiplying the geometric current density measured in the RRDE disk (*i.e.*, the j_{ORR} values displayed on Fig. 4) by the geometric area of the RRDE disk, $A_{Disk} \approx 0.238$ cm^2. I_r is the ring current and N = 0.39 is the collection efficiency of the RRDE ring (N is determined experimentally as

described elsewhere [48]). The dependence on E of the average number of electrons (n) that are exchanged during the ORR is shown in Fig. 5.

It is expected that the proposed ECs reduce O_2 to water by a 4-electron pathway. At E > 0.28 V *vs.* RHE, with respect to the Pt/C reference, the PtCo-CN$_l$ T$_f$/C$_w$ ECs are more selective towards the 4-electron pathway. The only clear exception is PtCo-CN$_l$ 900/C$_{1/4}$. This evidence is interpreted by considering that two adjacent Pt sites are needed for a 4-electron ORR process [49]. The adsorption of hydrogen species on the Pt/C reference at E < 0.4 V *vs.* RHE, that takes place preferentially on the surface defects, reduces the number of couples of neighboring Pt atoms decreasing the ORR selectivity in the 4-electron pathway. In the ECs here proposed, the size of the $PtCo_x$ NPs is significantly larger (see Table ESI1) in comparison with the Pt/C reference. Thus, the concentration of defects on the surface of the $PtCo_x$ alloy NPs is much lower. Consequently, the density of hydrogen species adsorbed on the surface of $PtCo_x$ NPs is lower, increasing the number of couples of neighbouring Pt atoms available for the 4-electron ORR pathway [49]. In PtCo-CN$_l$ 900/C$_{1/4}$, Co is strongly stabilized on the surface of $PtCo_x$ NPs by means of the N-based ligands of the CN matrix present on *"coordination nests"*, thus the density of available Pt neighboring couples on the NP surface is reduced, lowering the selectivity in the 4-electron ORR process. The ECSA of the PtCo-CN$_l$ T$_f$/C$_w$ ECs is determined as elsewhere described by normalizing the CO_{ad} stripping charge obtained from the integration of the profiles displayed in Fig. 3 to the value of 484 $\mu C \cdot cm_{Pt}^{-2}$, [50, 51]. Results are shown in Table 2.

The ECSA values of the PtCo-CN$_l$ T$_f$/C$_w$ ECs are significantly lower than that of the Pt/C reference. In particular, ECSA: (a) increases in the order PtCo-CN$_l$ 600/C$_{1/4}$ < PtCo-CN$_l$ 600/C$_{2/4}$ ≈ PtCo-CN$_l$ 600/C$_{4/4}$ < Pt/C reference; and (b) decreases on T$_f$ in PtCo-CN$_l$ T$_f$/C$_{1/4}$ ECs. This behavior can be explained on the basis of the hypothesis (see Section 3.1) that on **w** the Z-IOPE 3D-network of precursor expands reducing the density of crosslinking anionic clusters, which are then responsible,

during the pyrolysis process, of the metal nucleation, coalescence and growth of $PtCo_x$ NPs. These latter consecutive processes occur at T_f > 600 °C and are significantly dependent on the typical thermally-activated metal diffusion phenomena.

A quantitative evaluation of the ORR performance is carried out by removing the mass transport contribution from the disk current densities (j_{disk}) (Fig. 4). The faradic ORR current density, j_k, is given by [36]:

$$\frac{1}{j} = \frac{1}{j_k} + \frac{1}{j_d} \qquad (2)$$

where j_d is the current density at 0.2 V *vs.* RHE in the ORR profiles shown in Fig. 4. The faradic ORR current (i_k) is obtained by multiplying j_k by the geometric area of the glassy carbon disk electrode ($A_{Disk} \approx 0.238$ cm^2). i_k is adopted to determine the mass (i_m) and the specific (i_s) activity of ECs as elsewhere described [36]. i_m and i_s are displayed in Fig. 6. The values of i_m and i_s at 0.9 V *vs.* RHE are adopted to gauge the performance of the PtCo-CN_l T_f/C_w ECs in the ORR (see Table 2) [36]. In Fig. 6 two different behaviors can be observed: (i) at V < 0.85 V *vs.* RHE, the Tafel slope is ~120 mV·dec^{-1}, which is typical of a 4-electron ORR mechanism on oxide-free Pt surfaces; (ii) at V > 0.85 V *vs.* RHE, the Tafel slope is lower (~60 mV·dec^{-1}) owing to the coverage of Pt surfaces with oxide species [52, 53]. The Tafel slopes of PtCo-CN_l T_f/C_w are similar to those of the Pt/C reference, suggesting that in all the ECs the ORR occurs with the same 4-electron general mechanism. The main parameter affecting the $i_{m(0.9\ V)}$ values of PtCo-CN_l $T_f/C_{1/4}$ is T_f. PtCo-CN_l 600/$C_{1/4}$ shows a value of $i_{m(0.9\ V)}$ = 0.132 A·mg$_{Pt}^{-1}$, which is close to that of the Pt/C reference. On T_f, the values of $i_{m(0.9\ V)}$ of PtCo-CN_l $T_f/C_{1/4}$ decrease up to a factor of *ca.* 4-5, concurrently with the growth of the $PtCo_x$ NPs and the decrease of the ECSA (see Table 2). This study is completed by investigating $i_{s(0.9\ V)}$ values on sample treatments and composition [36]. $i_{s(0.9\ V)}$ values of proposed

ECs are 3.5 – 6 times larger with respect to that of the Pt/C reference, suggesting that both an electronic and a bifunctional effect is provided by the Co atoms alloyed in the $PtCo_x$ NPs [46, 54]. In detail, it is expected that the Co oxidized species present on the surface of alloy NPs create a suitable local acid environment which improves the rate and density of protonation processes of reaction intermediate species coordinated on the Pt active site. In this way, in active sites a high rate of $O_2 \rightarrow H_2O$ direct processes occur owing to the fast desorption of O_2 reduction products [33, 37]. In PtCo-CN_l $T_f/C_{1/4}$ ECs, the best compromise between $i_{m(0.9\ V)}$ and $i_{s(0.9\ V)}$ is obtained at T_f = 600°C (see Table 2). This *"optimal"* T_f is adopted in order to study the effects of **w** on the performance of ECs. Table 2 shows that $i_{m(0.9\ V)}$ of PtCo-CN_l $600/C_w$ ECs increases on **w** in accordance with the behavior of: (i) ECSA, which increases in the order PtCo-CN_l $600/C_{1/4}$ < PtCo-CN_l $600/C_{2/4}$ ≈ PtCo-CN_l $600/C_{4/4}$ (see Table 2); and (ii) $i_{s(0.9\ V)}$, that rises from PtCo-CN_l $600/C_{2/4}$ to PtCo-CN_l $600/C_{4/4}$. Taken all together, the *"ex-situ"* studies demonstrate that PtCo-CN_l $600/C_{4/4}$ is the best ORR EC and support the interpretation described in Section 3.1.

3.5.2. Performance in single PEMFC

Fig. 7 reports the polarization and power curves of the proposed ECs, which are tested in PEMFCs operating under *"ideal"* conditions *i.e.*, with the cathode fed with pure oxygen at a BP of 4 bar. The overall performance of the PtCo-CN_l $T_f/C_{1/4}$ ECs is quite similar to that of the Pt/C reference (see the left panels of Fig. 7). At high cell potentials, and in particular at a cell potential of 0.6 V, the mass power yielded by PtCo-CN_l $T_f/C_{1/4}$ ECs increases in the order: PtCo-CN_l $900/C_{1/4}$ (1140 $W \cdot g_{Pt}^{-1}$) < Pt/C ref. (1200 $W \cdot g_{Pt}^{-1}$) < PtCo-CN_l $700/C_{1/4}$ (1345 $W \cdot g_{Pt}^{-1}$) < PtCo-CN_l $500/C_{1/4}$ (1650 $W \cdot g_{Pt}^{-1}$) < PtCo-CN_l $600/C_{1/4}$ (1720 $W \cdot g_{Pt}^{-1}$). This trend is consistent with results obtained by CV-TF-RRDE measurements (see Table 2) and confirm that PtCo-CN_l $600/C_{1/4}$ exhibits the best overall performance, also in comparison with that of the Pt/C reference. The data shown in the left panels of Fig. 7 also indicate that the optimal T_f is 600 °C, while the results of the right panels of Fig. 7 confirm that, in *"ideal"* operating conditions, **w** does not affect significantly the overall

performance of the ECs. At high cell potentials, and in particular at a cell potential of 0.6 V, the mass power yielded by the ECs obtained at T_f = 600 °C exhibits the following trend: Pt/C reference (1200 $W \cdot g_{Pt}^{-1}$) < PtCo-CN_l 600/$C_{4/4}$ (1500 $W \cdot g_{Pt}^{-1}$) < PtCo-CN_l 600/$C_{1/4}$ (1720 $W \cdot g_{Pt}^{-1}$) < PtCo-CN_l 600/$C_{2/4}$ (1750 $W \cdot g_{Pt}^{-1}$). These results highlight a discrepancy with the outcome of RRDE measurements. Indeed, in single PEMFC the best performance is obtained by PtCo-CN_l 600/$C_{2/4}$, while in RRDE the best EC is PtCo-CN_l 600/$C_{4/4}$ (see Table 2 and the end of Section 3.5.1.). In principle, this discrepancy could be ascribed to the presence in ECs of charge and mass transport issues, that hardly affect the RRDE measurements [55] and which are crucial in the determination of PEMFC performance [39, 56]. In first approximation the proposed ECs comprise a support that includes the same amounts of C and N (*ca.* 80 and less than 1.5 wt%, respectively; see Table 1). Hence, owing to the low wt% of N it is reasonable to admit that the ECs here described exhibit a very high electrical conductivity. Thus, it is expected that they will show no appreciable ohmic drop in the polarization curves [26]. On these bases, it is concluded that the performance of these materials in PEMFC is mostly modulated by the mass transport phenomena. These latter events, which are strongly correlated to the morphology of the ECs [39], are studied by analyzing the polarization curves as a function of the P_{O_2} at the cathode feed [39, 57]. Polarization curves shown in Fig. 8 are measured feeding the cathode with air at a back pressure of 4 bar. The performance of the ECs is also registered by using in the cathode feed a back pressure of 1 bar with: (i) pure O_2; and (ii) air. Results obtained under (i) and (ii) conditions are respectively displayed in Fig. ESI2 and Fig. ESI3 reported in Electronic Supplementary Information.

Fig. 8 shows clearly that, as the P_{O_2} in the cathode feed is lowered, the performance in the ORR of the proposed ECs drops below that of the Pt/C reference. A semiquantitative approach to gauge the impact of the mass transport phenomena on the performance of the ECs consists in studying the dependence of the maximum mass power (MMP) on P_{O_2} in the cathode feed [39]. It is highlighted

that the MMP of a PEMFC is typically measured at a current density of the order of few hundreds of $mA \cdot cm^{-2}$ (see Fig. 7 and Fig. 8). In these conditions, in the cathode per unit time a large amount of: (i) oxygen is consumed; and (ii) water is produced. Hence, the empirical approach here described is useful to study the impact of *"mass transport phenomena"* on PEMFC in terms of: (i) the migration process of oxygen towards the ORR active sites; and (ii) the elimination of water product from the active sites. The method consists in the determination of four empirical parameters by means of the following Equation (3):

$$\Psi_{\frac{H}{L}} = \frac{MMP_H}{MMP_L} \quad (3)$$

where H and L indicate the operating conditions of the cathode feed: H, L = O4 (pure O_2 at BP = 4 bar); O1 (pure O_2 at BP = 1 bar); A4 (air at BP = 4 bar); A1 (air at BP = 1 air). In Table 3 are summarized the four empirical parameters, $\Psi_{O4/A4}$; $\Psi_{O1/A1}$; $\Psi_{O4/O1}$ and $\Psi_{A4/A1}$, whose values: (i) increase as the mass transport of reactants and products to and from the active sites becomes more hindered [39]; and (ii) show an asymptotic tendency to 1 as the effect of the mass transport phenomena on the ORR is decreased. On these bases the $\Psi_{O4/A4}$, $\Psi_{O1/A1}$, $\Psi_{O4/O1}$ and $\Psi_{A4/A1}$ parameters provide a comprehensive picture on the effect of P_{O_2} on the ORR performance of the ECs in a broad range of operating conditions. The mass transport information represented by $\Psi_{O4/A4}$, $\Psi_{O1/A1}$, $\Psi_{O4/O1}$ and $\Psi_{A4/A1}$ parameters can be summarized into a single averaged empirical parameter *"Ψ_{av}"*, which accounts for the *"average accessibility"* of reagents towards the active sites. In addition, Table 3 reveals that Ψ_{av} values: (i) of the proposed ECs are higher than that of the Pt/C reference; (ii) in PtCo-CN_l $T_f/C_{1/4}$ ECs are at minimum when 600 °C < T_f < 700 °C; and (iii) in PtCo-CN_l $600/C_w$ ECs are minimized when **w** = 2/4.

To explain this behavior it is necessary to consider that the ECs here proposed include up to *ca.* 10 wt% of $PtCo_x$ NPs (see Table 1), which exhibit a size of *ca.* 8 nm or more (see Fig. 2 and Table ESI1 in Electronic Supplementary Information). On the other hand, the Pt/C reference bears 20 wt% of Pt (see Section 2.1) with a NP average size of *ca.* 3 nm, which is supported on spherical carbon NPs (XC-72R) [33, 39]. This information suggests that, with respect to the Pt/C reference, the ECSA of PtCo-CN_l T_f/C_w ECs would be significantly lower (see Table 2). Furthermore, tests in PEMFC of ECs are performed loading the cathode of the membrane-electrode assemblies with the same amount of Pt (*i.e.*, 0.1 $mg_{Pt} \cdot cm^{-2}$, see Section 2.5). Results show that: (i) the volumetric density of the ORR active sites decreases in the following order: Pt/C reference > PtCo-CN_l T_f/C_w; and (ii) for PtCo-CN_l T_f/C_w ECs, a significant inhibition of the oxygen diffusion process by the CN *"shell"* is revealed (see Section 3.1 and Fig. 2). Taking all together, with respect to the Pt/C reference, Ψ_{av} of ECs are higher (see Table 3), thus witnessing that oxygen transport in these materials is more difficult.

Furthermore, PtCo-CN_l $900/C_{1/4}$ EC shows: (i) very large $PtCo_x$ NPs (grain sizes higher than *ca.* 30 nm, see Table ESI1 in Electronic Supplementary Information); and (ii) the smallest ECSA value (see Table 2). In addition, in the cathodic layers of PtCo-CN_l $T_f/C_{1/4}$ ECs: (i) the volumetric concentration of ORR active sites shows a minimum at T_f = 900 °C (Ψ_{av} = 2.86, see Table 3); and (ii) the size of $PtCo_x$ NPs is the smallest at T_f = 500 °C (grain size of *ca.* 8 nm, see Table ESI1 in Electronic Supplementary Information, corresponding to the largest value of ECSA, see Table 2; Ψ_{av} = 2.98). Hence, it is concluded that in PtCo-CN_l $500/C_{1/4}$ the volumetric concentration of ORR active sites is actually maximized, but the transport of reactants and products to and from the ORR active sites is poor. This apparent discrepancy can be rationalized considering that at T_f = 500 °C the graphitization of the CN *"shell"* of PtCo-CN_l $500/C_{1/4}$ is likely not complete, in compliance with the results obtained on other similar systems obtained at a pyrolysis temperature of 500 °C

[29]. Hence, in PtCo-CN_l 500/$C_{1/4}$ the ORR active sites are clogged by functional groups present in the CN matrix. PtCo-CN_l T_f/$C_{1/4}$ ECs in the range 600 °C < T_f < 700 °C show the lowest Ψ_{av} values likely owing to their: (i) volumetric concentration of ORR active sites, which in the CN *"shell"* is sufficiently large; and (ii) *"degree of graphitization"* of the CN *"shell"*, which is practically completed (the ligands of the CN matrix clogging the ORR active sites are removed). The graphitization of the CN *"shell"* depends on T_f [26, 29], thus the T_f parameter is inversely related to the density of functional groups remaining after the pyrolysis on the CN-matrix. In addition, the Ψ_{av} values of PtCo-CN_l 600/$C_{1/4}$, PtCo-CN_l 600/$C_{2/4}$ and PtCo-CN_l 600/$C_{4/4}$ clearly indicate that the clogging of active sites by the functional groups present on the surface of the CN matrix is not the only one factor affecting the accessibility of reactants or products to and from the ORR active sites.

The ECSA of the PtCo-CN_l 600/C_w ECs, which are composed with a wt% of both Pt and Co similar to that of other ECs (see Table 1), increases in the order PtCo-CN_l 600/$C_{1/4}$ < PtCo-CN_l 600/$C_{2/4}$ ≈ PtCo-CN_l 600/$C_{4/4}$ (see Table 2). This behavior for these systems supports the structural interpretation described in Section 3.1 and shown in Fig. 2. Taking all together, the volumetric densities of the ORR active sites in the CN *"shells"* of PtCo-CN_l 600/$C_{2/4}$ and PtCo-CN_l 600/$C_{4/4}$ are: (i) very similar; and (ii) larger than that of PtCo-CN_l 600/$C_{1/4}$, which exhibits poor mass transport features (Ψ_{av} = 2.67, see Table 3). However, with respect to PtCo-CN_l 600/$C_{2/4}$, PtCo-CN_l 600/$C_{4/4}$ shows a higher Ψ_{av} (2.89 *vs.* 2.35, see Table 3), thus demonstrating that, with respect to PtCo-CN_l 600/$C_{2/4}$, the ORR active sites of PtCo-CN_l 600/$C_{4/4}$ are embedded into a more compact CN *"shell"*. In summary, in the high-current regime the best EC is PtCo-CN_l 600/$C_{2/4}$, in terms of: (i) mass transport phenomena; (ii) mass power at a cell potential of 0.6 V (1750 $W \cdot g_{Pt}^{-1}$); and (iii) maximum mass power (2481 $W \cdot g_{Pt}^{-1}$). It is further noted that these latter two metrics in the proposed ECs are actually improved in comparison with the Pt/C reference, that exhibits a mass

power at a cell potential of 0.6 V and a maximum mass power equal to 1200 $W \cdot g_{Pt}^{-1}$ and 2325 $W \cdot g_{Pt}^{-1}$, respectively.

A further study of the performance of ECs in single PEMFCs is performed by analyzing on sample composition and T_f the dependence of the cell potential at a specific current of 50 $A \cdot g_{Pt}^{-1}$ [39]. In these conditions the current density yielded by the PEMFC is 12 $mA \cdot cm^{-2}$. This value is *ca.* 1-2 orders of magnitude lower than that of the current density measured at the maximum mass power of the PEMFC (see above). Therefore, under these kinetic operating conditions the ECs yield very little water and shows very small and practically constant ohmic drops. Under these conditions the PEMFC performance (see the caption of Fig. 7) is mainly controlled by: (i) the intrinsic ORR kinetics of the cathode EC; and (ii) the local P_{O_2} on the ORR active sites [39, 58], which depends on the transport phenomena of oxygen in the immediate neighborhood of the active sites. Table 4 summarizes the cell potentials of ECs in PEMFCs measured at a specific current of 50 $A \cdot g_{Pt}^{-1}$ and at different values of P_{O_2}.

In pure O_2 at a back pressure of 4 bar [O_2, 4 bar] the values of V@50 $A \cdot g_{Pt}^{-1}$ are diagnostic of the kinetic performance of the ECs. In this latter condition the mass transport phenomena can be neglected. V@50 $A \cdot g_{Pt}^{-1}$ [O_2, 4 bar] values can be correlated to the ORR kinetic parameters determined by CV-TF-RRDE measurements (see Section 3.5.1.). For the sake of comparison, results of electrochemical tests are obtained keeping constant the loading of Pt: (i) 0.1 $mg_{Pt} \cdot cm^{-2}$ for the PEMFC cathode; and (ii) 12 $\mu g \cdot cm^{-2}$ for RRDE measurements (see Section 2.5. and Section 2.4., respectively). Table 4 summarizes the values of V@50 $A \cdot g_{Pt}^{-1}$ [O_2, 4 bar], obtained in PEMFC tests, while Table 2 shows the $i_{m(0.9\ V)}$ values determined by CV-TF-RRDE. In these conditions results obtained with these two radically different experimental setups are very similar. In particular, the performance of PtCo-CN_l $T_f/C_{1/4}$ ECs decreases on T_f and that of PtCo-CN_l $600/C_{2/4}$

is improved with respect to both the Pt/C reference and the PtCo-CN_l 600/$C_{1/4}$ EC. This evidence confirms that CV-TF-RRDE measurements are able to provide a reliable first estimate of the kinetic performance of an ORR EC and that, in first approximation, the ORR performance of the proposed ECs has been successfully transferred from an *"ex-situ"* electrochemical environment to an *"in-situ"* single PEMFC application. A comparison of the results shown in Table 2 with those reported in Table 4 indicates that the performance in CV-TF-RRDE increases in the order PtCo-CN_l 600/$C_{2/4}$ < PtCo-CN_l 600/$C_{4/4}$, while the reverse trend is detected in single PEMFC. This discrepancy confirms the structural hypothesis described in Section 3.1. Indeed, in compliance with the above observations, with respect to PtCo-CN_l 600/$C_{2/4}$, the ORR active sites of PtCo-CN_l 600/$C_{4/4}$ are embedded into a more compact CN *"shell"* which inhibits the transport of oxygen to the active sites even at low ORR currents. This phenomenon, which is associated to the presence on the active sites of a P_{O_2} lower than that externally imposed, reduces significantly V@50 $A \cdot g_{Pt}^{-1}$ [O_2, 4 bar].

This evidence suggests that, even though V@50 $A \cdot g_{Pt}^{-1}$ values are determined at very low current densities, the transport phenomena of the ORR reactants and products towards or from the active sites play a crucial role in determining the ORR performance of the ECs in a PEMFC. In order to better gauge these effects, in this work we studied the $\Delta_{H/L}$ empirical parameters. Each $\Delta_{H/L}$ is defined as the difference between the V@50 $A \cdot g_{Pt}^{-1}$ values measured when the cathode is fed with oxygen in the H and L conditions. The H and L conditions are consistent with those defined above for $\Psi_{H/L}$ (see Equation (3)). The values and the detailed definitions of $\Delta_{O4/A4}$, $\Delta_{O1/A1}$, $\Delta_{O4/O1}$ and $\Delta_{A4/A1}$ parameters are shown in Table 4. A large value of $\Delta_{H/L}$ indicates that a significant decrease of V@50 $A \cdot g_{Pt}^{-1}$ is registered as P_{O_2} is reduced. For instance, $\Delta_{O4/A4}$ corresponds to the decrease in V@50 $A \cdot g_{Pt}^{-1}$ *"upon changing the cathode feed from pure oxygen to air as the overall BP is kept constant at 4 bar"*. In accordance with $\Psi_{H/L}$ parameters (H/L = O4/A4, O1/A1, O4/O1, A4/A1), a negligible influence on the performance of the PEMFC of the mass transport phenomena

corresponds to a *"small"* value of the $\Delta_{H/L}$ parameter. Furthermore, also in this case the information of the $\Delta_{O4/A4}$, $\Delta_{O1/A1}$, $\Delta_{O4/O1}$ and $\Delta_{A4/A1}$ empirical parameters can be summarized into a single averaged parameter, labelled *"Δ_{av}"* (see the caption of Table 4). The behavior of Ψ_{av} and Δ_{av} on EC composition and T_f shows that these parameters are correlated to each other and that: (i) increase in the order Pt/C reference < all the PtCo-CN$_l$ T_f/C_w ECs; (ii) in PtCo-CN$_l$ T_f/$C_{1/4}$, are minimized for 600 °C < T_f < 700 °C; and (iii) are very similar for PtCo-CN$_l$ 600/$C_{1/4}$ and PtCo-CN$_l$ 600/$C_{4/4}$. These insights suggest that the structural and morphological features affect the mass transport properties of ECs in PEMFC tests in the same way both in the *"low-current"* and in the *"high-current"* regime. It is noted that in PtCo-CN$_l$ 600/C_w ECs, the minimum Ψ_{av} is registered at **w** = 2/4 (see Table 3) while Δ_{av} does not change significantly among the various samples (see Table 4). This evidence is rationalized considering that the Pt/N molar ratio of PtCo-CN$_l$ 600/$C_{2/4}$ is significantly larger with respect to that of both PtCo-CN$_l$ 600/$C_{1/4}$ and PtCo-CN$_l$ 600/$C_{4/4}$ (2.2 *vs. ca.* 1.6, see Table 1). Thus, it is expected that a high N concentration at the interface [CN-matrix]/[$PtCo_x$ NPs] stabilizes on the surface of alloy NPs the hydrophilic Co species, which facilitate the absorption of water promoting the formation of solvation shells covering the metal active sites (partial flooding of active sites). This effect degrades the O_2 transport features toward active sites of PtCo-CN$_l$ 600/$C_{2/4}$ EC and limit the positive effects associated in this material to a more porous CN *"shell"*. However, at large current densities this phenomenon is not particularly evident, probably owing to the following reasons: (i) the larger amount of water produced at the ORR active sites originates a high water concentration gradient, which facilitates its elimination; and (ii) the ORR active sites at high P_{O_2} and gas flow rates promote the desorption processes of water molecules.

Taken all together, in the low-current regime the most promising EC is PtCo-CN$_l$ 600/$C_{2/4}$. Indeed, it exhibits a V@50 A·g_{Pt}^{-1} [O_2, 4 bar] equal to 908 mV. This value is more than 20 mV higher than that of the Pt/C reference (see Table 4). This result confirms the outcome of CV-TF-RRDE

measurements (see Table 2) and witnesses that, with respect to the Pt/C reference, PtCo-CN_l 600/$C_{2/4}$ is also able to yield an improved ORR kinetics in a PEMFC. Finally, PtCo-CN_l 600/$C_{2/4}$ reveals one of the lowest Δ_{av} values among the ECs here presented (see Table 4) demonstrating that it is characterized by acceptable mass transport features.

4. Conclusions

This report shows that the performance in the ORR of the *"core-shell"* CN-based ECs here described depends on: (i) the structure, composition and interactions of the nanocomposite zeolitic inorganic-organic polymer electrolyte precursor used (nZ-IOPE); and (ii) the parameters characterizing the pyrolysis process. In a first series of experiments T_f is optimized. The best ORR performance, as determined by CV-TF-RRDE measurements, is obtained at T_f = 600 °C. The mass ratio *"**w**"* between the sucrose binder and the carbon black used in the synthesis of the nZ-IOPE precursor is then modulated between 1/4 and 4/4.

It is revealed that upon the pyrolysis process: (i) the carbon NPs originally introduced in the nZ-IOPE precursor form the *"core"* of the ECs; (ii) the precursor Z-IOPE domains undergo graphitization, forming a CN *"shell"* that wraps the *"core"*; and (iii) $PtCo_x$ NPs nucleate and grow in the CN *"shell"*. This general picture is corroborated by the morphological analysis carried out by HR-TEM (see Fig. 2). The $PtCo_x$ NPs are stabilized into the *"shell"* by means of *"coordination nests"* based on C- and N- ligands. N atoms are introduced in the ECs by means of the cyano ligands of the $Co(CN)_6^{3-}$ complex used in the synthesis of the nZ-IOPE precursor, which are strongly bound to the Co metal center [59]. For this reason the N atoms in ECs should be located in close proximity to Co atoms coalesced into the $PtCo_x$ NPs. The features of the final ECs are strongly dependent on the structure of the starting nZ-IOPE precursor, which in turn is significantly modulated by the mass ratio **w**. At large values of **w**, sucrose segregates inside the interstices of the 3D Z-IOPE network. Thus, the density of the hybrid inorganic-organic network decreases, reducing the amount of Pt and Co species that can coalesce into each $PtCo_x$ NP during the pyrolysis process. As **w** = 1/4, the largest part of sucrose is involved in the formation of the 3D network of the Z-IOPE and only few small sucrose domains are formed. As a result: (i) large domains comprising anionic metal clusters are available to feed the nucleation and growth processes of large $PtCo_x$ NPs; and (ii) a compact CN matrix is obtained. These latter features inhibit the diffusion of oxygen to the surface

of the $PtCo_x$ NPs, reducing the O_2 accessibility to the active sites. For **w** = 2/4, larger sucrose domains are formed, which expand the 3D network of Z-IOPE precursor. This reduces the local availability of metal species able to coalesce into $PtCo_x$ NPs and promotes the production of a more porous CN *"shell"* which improves the accessibility of O_2 towards the active sites. In this case, a lower Ψ_{av} value is obtained. Finally, as sucrose is increased (**w** = 4/4), the large sucrose domains embedded in the 3D network of the Z-IOPE precursor give rise to: (i) smaller $PtCo_x$ NPs; (ii) a high value of Ψ_{av}, demonstrating that a more compact CN *"shell"* is obtained when the 3D hybrid structure of Z-IOPE precursor collapses stimulated by the degradation of the large sucrose domains.

The electrochemical studies performed by CV-TF-RRDE measurements show that the ECSA of the ECs increases in the order PtCo-CN_l 600/$C_{1/4}$ (10.3 $m^2 \cdot g_{Pt}^{-1}$) < PtCo-CN_l 600/$C_{2/4}$ (28.1 $m^2 \cdot g_{Pt}^{-1}$) ≈ PtCo-CN_l 600/$C_{4/4}$ (25.6 $m^2 \cdot g_{Pt}^{-1}$). In addition, it is determined that, with respect to the Pt/C reference, the intrinsic activity in the ORR of the proposed ECs in acid medium is improved by a factor of 3.5 – 6. This result is rationalized considering that the Co atoms alloyed into the $PtCo_x$ NPs give rise: (i) to strain phenomena promoting the ORR kinetics by means of electronic effects [45]; (ii) to oxophilic Co species, that are stabilized on the surface of $PtCo_x$ NPs by the C- and N-ligands of the *"coordination nests"* and promote the ORR by means of *"bifunctional effects"* [34]. CV-TF-RRDE demonstrates that the best EC is PtCo-CN_l 600/$C_{4/4}$, which provides: (i) the best compromise between ECSA and intrinsic activity; and (ii) the highest mass activity at 0.9 V *vs.* RHE (0.304 $A \cdot g_{Pt}^{-1}$) in comparison with that of the Pt/C reference (0.161 $A \cdot g_{Pt}^{-1}$).

This report reveals that mass transport issues arising from the morphology, the structure and the chemical composition of the ECs strongly affect the PEMFC performance. It is demonstrated that even though CV-TF-RRDE studies provide good preliminary insights on ORR kinetics, mass transport issues influence significantly the EC performance in an operating PEMFC even at low

current densities and at high P_{O_2}. In this regard a number of morphological and chemical features are identified, that are responsible to modulate the mass transport phenomena in both the *"high-"* and *"low-current"* regime. In general, the mass transport phenomena are facilitated as the ORR active sites: (i) exhibit a high volumetric density; (ii) are not embedded into a compact CN *"shell"*; and (iii) are not clogged by ligands derived from the incomplete graphitization of the nZ-IOPE precursor. It is also found that the chemical interactions between the CN matrix and the $PtCo_x$ NPs affect the mass transport phenomena and the strong hydrophilic environment created in the EC surface by Co oxophilic species. These latter, which are stabilized by the nitrogen ligands of the CN *"shell"*, facilitate the absorption and the aggregation of water molecules on the surface of alloy NPs to form the solvation shell which covers the active sites. This phenomenon is particularly evident at low current densities and is responsible of the initial flooding processes of the ORR active sites.

Taken all together, the ECs presented in this report exhibit a promising performance, both in a CV-TF-RRDE setup and in single PEMFC. In particular, PtCo-CN_l 600/$C_{2/4}$ reveals the best performance in single PEMFC. In *"ideal"* operating conditions, the PEMFC mounting PtCo-CN_l 600/$C_{2/4}$ at the cathode exhibits a V@50 $A \cdot g_{Pt}^{-1}$ equal to 908 mV and yields a mass power of 1750 $W \cdot g_{Pt}^{-1}$ at a cell potential of 0.6 V. These metrics are improved in comparison with the PEMFC mounting the Pt/C reference, that exhibits a V@50 $A \cdot g_{Pt}^{-1}$ equal to 884 mV and yields a mass power of 1200 $W \cdot g_{Pt}^{-1}$ at a cell potential of 0.6 V. The structural features of the nZ-IOPE precursor are crucial in the modulation of the final properties of ECs and affect: (i) the trends observed in the ORR performance; and (ii) the discrepancies between the results achieved in the CV-TF-RRDE setup and in single PEMFC. In conclusion, this report summarizes a study carried out to understand the fundamental mechanisms that modulate the interplay between the synthetic parameters, the physicochemical properties and the electrochemical performance of the ECs obtained with the proposed preparation route.

On the whole, the present results are consistent with previous observations made for originally inert graphene in which the catalytically active sites were formed by replacement of the lattice carbons with such heteroatoms as nitrogen [60, 61]. Consequently, differences in the oxygen adsorption, activation and its reductive activity were postulated. Strong interactions between Pt as well as alloy-forming metals (e.g. Co) and N-derivatized units (within nanopores) were suggested to explain the observed electrocatalytic enhancement effects.

Acknowledgements

This project has received funding from: (a) the European Union's Horizon 2020 research and innovation programme under grant agreement Graphene Core 2 785219; (b) the program *"Budget Integrato per la Ricerca Interdipartimentale - BIRD 2018"* of the University of Padova (protocol BIRD187913); (c) the project *"Hierarchical electrocatalysts with a low platinum loading for low-temperature fuel cells – HELPER"* funded by the University of Padova. Partial support from the National Science Center (NCN, Poland) under Opus Project 2018/29/B/ST5/02627 is also appreciated by PJK and IAR.

References

[1] I. Katsounaros, S. Cherevko, A.R. Zeradjanin, K.J.J. Mayrhofer, Oxygen electrochemistry as a cornerstone for sustainable energy conversion, Angewandte Chemie - International Edition, 53 (2014) 102-121.

[2] F. Cheng, J. Chen, Metal-air batteries: From oxygen reduction electrochemistry to cathode catalysts, Chemical Society Reviews, 41 (2012) 2172-2192.

[3] M. Shao, Q. Chang, J.P. Dodelet, R. Chenitz, Recent Advances in Electrocatalysts for Oxygen Reduction Reaction, Chemical Reviews, 116 (2016) 3594-3657.

[4] B. Dunn, H. Kamath, J.M. Tarascon, Electrical energy storage for the grid: A battery of choices, Science, 334 (2011) 928-935.

[5] Energy infrastructure priorities for 2020 and beyond - A Blueprint for an integrated European energy network, European Commission, Brussels, 2010.

[6] Energy 2020 - A strategy for competitive, sustainable and secure energy, COM(2010) 639, European Commission, Brussels, 2010.

[7] N. Quental, D. Buttle, S. Abrar, K. Firkaviciuté, J. Jimenez Mingo, D. Sofianopoulos, A. Kontoudakis, C. Sales Agut, The Strategic Energy Technology (SET) Plan, Publications Office of the European Union, Luxembourg, 2017.

[8] R. O'Hayre, S.W. Cha, W. Colella, F.B. Printz, Fuel Cell Fundamentals, John Wiley & Sons, Hoboken, 2006.

[9] S. Rodosik, J.P. Poirot-Crouvezier, Y. Bultel, Impact of humidification by cathode exhaust gases recirculation on a PEMFC system for automotive applications, International Journal of Hydrogen Energy, 44 (2018) 12802-12817.

[10] V. Vielstich, Ideal and effective efficiencies of cell reactions and comparison to carnot cycles, in: V. Vielstich, A. Lamm, H.A. Gasteiger (Eds.) Handbook of Fuel Cells - Fundamentals, Technology and Applications, John Wiley & Sons, Chichester, 2003, pp. 26-30.

[11] G. Hinds, E. Brightman, Towards more representative test methods for corrosion resistance of PEMFC metallic bipolar plates, International Journal of Hydrogen Energy, 40 (2015) 2785-2791.

[12] Z.F. Li, L. Xin, F. Yang, Y. Liu, H. Zhang, L. Stanciu, J. Xie, Hierarchical polybenzimidazole-grafted graphene hybrids as supports for Pt nanoparticle catalysts with excellent PEMFC performance, Nano Energy, 16 (2015) 281-292.

[13] Z.Q. Tian, S.H. Lim, C.K. Poh, Z. Tang, Z. Xia, Z. Luo, P.K. Shen, D. Chua, Y.P. Feng, Z. Shen, J. Lin, A Highly Order-Structured Membrane Electrode Assembly with Vertically Aligned Carbon Nanotubes for Ultra-Low Pt Loading PEM Fuel Cells, Advanced Energy Materials, 1 (2011) 1205-1214.

[14] 3.4 Fuel Cells, 2016, https://energy.gov/sites/prod/files/2017/05/f34/fcto_myrdd_fuel_cells.pdf (accessed 20 December 2017).

[15] M. Kiani, J. Zhang, Y. Luo, C. Jiang, J. Fan, G. Wang, J. Chen, R. Wang, Recent developments in electrocatalysts and future prospects for oxygen reduction reaction in polymer electrolyte membrane fuel cells, Journal of Energy Chemistry, 27 (2018) 1124-1139.

[16] M. Zhou, H.L. Wang, S. Guo, Towards high-efficiency nanoelectrocatalysts for oxygen reduction through engineering advanced carbon nanomaterials, Chemical Society Reviews, 45 (2016) 1273-1307.

[17] C.R. Raj, A. Samanta, S.H. Noh, S. Mondal, T. Okajima, T. Ohsaka, Emerging new generation electrocatalysts for the oxygen reduction reaction, Journal of Materials Chemistry A, 4 (2016) 11156-11178.

[18] N. Todoroki, R. Sasakawa, K. Kusunoki, T. Wadayama, Oxygen Reduction Reaction Activity of Nano-Flake Carbon-Deposited $Pt_{75}Ni_{25}$(111) Surfaces, Electrocatalysis, 10 (2019) 232-242.

[19] D. Liu, L. Tao, D. Yan, Y. Zou, S. Wang, Recent Advances on Non-precious Metal Porous Carbon-based Electrocatalysts for Oxygen Reduction Reaction, ChemElectroChem, 5 (2018) 1775-1785.

[20] T. Sun, B. Tian, J. Lu, C. Su, Recent advances in Fe (or Co)/N/C electrocatalysts for the oxygen reduction reaction in polymer electrolyte membrane fuel cells, Journal of Materials Chemistry A, 5 (2017) 18933-18950.

[21] U. Martinez, S. Komini Babu, E.F. Holby, P. Zelenay, Durability challenges and perspective in the development of PGM-free electrocatalysts for the oxygen reduction reaction, Current Opinion in Electrochemistry, 9 (2018) 224-232.

[22] S. Huang, A. Shan, R. Wang, Low pt alloyed nanostructures for fuel cells catalysts, Catalysts, 8 (2018).

[23] J. Park, L. Zhang, S.I. Choi, L.T. Roling, N. Lu, J.A. Herron, S. Xie, J. Wang, M.J. Kim, M. Mavrikakis, Y. Xia, Atomic layer-by-layer deposition of platinum on palladium octahedra for enhanced catalysts toward the oxygen reduction reaction, ACS Nano, 9 (2015) 2635-2647.

[24] N.K. Chaudhari, J. Joo, B. Kim, B. Ruqia, S.I. Choi, K. Lee, Recent advances in electrocatalysts toward the oxygen reduction reaction: The case of PtNi octahedra, Nanoscale, 10 (2018) 20073-20088.

[25] J. Qian, M. Shen, S. Zhou, C.-T. Lee, M. Zhao, Z. Lyu, Z.D. Hood, M. Vara, K.D. Gilroy, K. Wang, Y. Xia, Synthesis of Pt nanocrystals with different shapes using the same protocol to optimize their catalytic activity toward oxygen reduction, Materials Today, 21 (2018) 834-844.

[26] V. Di Noto, E. Negro, K. Vezzù, F. Bertasi, G. Nawn, Origins, Developments and Perspectives of Carbon Nitride-Based Electrocatalysts for Application in Low-Temperature FCs, The Electrochemical Society Interface, Summer 2015 (2015) 59-64.

[27] V. Di Noto, E. Negro, Core-shell mono/plurimetallic carbon nitride based electrocatalysts for low-temperature fuel cells (PEMFCs, DMFCs, AFCs and electrolysers), 2009.

[28] V. Di Noto, A novel polymer electrolyte based on oligo(ethylene glycol) 600, K_2PdCl_4, and $K_3Fe(CN)_6$, Journal of Materials Research, 12 (1997) 3393-3403.

[29] V. Di Noto, E. Negro, R. Gliubizzi, S. Gross, C. Maccato, G. Pace, Pt and Ni Carbon Nitride electrocatalysts for the oxygen reduction reaction, Journal of the Electrochemical Society, 154 (2007) B745-B756.

[30] E. Negro, K. Vezzù, F. Bertasi, P. Schiavuta, L. Toniolo, S. Polizzi, V. Di Noto, Interplay between Nitrogen Concentration, Structure, Morphology, and Electrochemical Performance of PdCoNi "Core-Shell" Carbon Nitride Electrocatalysts for the Oxygen Reduction Reaction, ChemElectroChem, 1 (2014) 1359-1369.

[31] E. Negro, A. Nale, K. Vezzù, G. Pagot, S. Polizzi, R. Bertoncello, A. Ansaldo, M. Prato, F. Bonaccorso, I.A. Rutkowska, P.J. Kulesza, V. Di Noto, Hierarchical oxygen reduction reaction electrocatalysts based on $FeSn_{0.5}$ species embedded in carbon nitride-graphene based supports, Electrochimica Acta, 280 (2018) 149-162.

[32] K. Vezzù, A. Bach Delpeuch, E. Negro, S. Polizzi, G. Nawn, F. Bertasi, G. Pagot, K. Artyushkova, P. Atanassov, V. Di Noto, Fe-carbon nitride *"Core-shell"* electrocatalysts for the oxygen reduction reaction, Electrochimica Acta, 222 (2016) 1778-1791.

[33] V. Di Noto, E. Negro, S. Polizzi, F. Agresti, G.A. Giffin, Synthesis-structure-morphology interplay of bimetallic *"core- shell"* carbon nitride nano-electrocatalysts, ChemSusChem, 5 (2012) 2451-2459.

[34] E. Negro, S. Polizzi, K. Vezzù, L. Toniolo, G. Cavinato, V. Di Noto, Interplay between morphology and electrochemical performance of *"core-shell"* electrocatalysts for oxygen reduction reaction based on a $PtNi_x$ carbon nitride *"shell"* and a pyrolyzed polyketone nanoball *"core"*, International Journal of Hydrogen Energy, 39 (2014) 2828-2841.

[35] V. Di Noto, E. Negro, R. Gliubizzi, S. Lavina, G. Pace, S. Gross, C. Maccato, A Pt-Fe Carbon Nitride Nano-electrocatalyst for Polymer Electrolyte Membrane Fuel Cells and Direct-Methanol Fuel Cells: Synthesis, Characterization and Electrochemical Studies, Advanced Functional Materials, 17 (2007) 3626-3638.

[36] H.A. Gasteiger, S.S. Kocha, B. Sompalli, F.T. Wagner, Activity benchmarks and requirements for Pt, Pt-alloy, and non-Pt oxygen reduction catalysts for PEMFCs, Applied Catalysis B: Environmental, 56 (2005) 9-35.

[37] V. Di Noto, E. Negro, Pt–Fe and Pt–Ni Carbon Nitride-Based 'Core–Shell' ORR Electrocatalysts for Polymer Electrolyte Membrane Fuel Cells, Fuel Cells, 10 (2010) 234-244.

[38] F. Basolo, R.G. Pearson, Mechanisms of Inorganic Reactions, 2nd ed., John Wiley & Sons Inc, Chichester, 1967.

[39] V. Di Noto, E. Negro, S. Polizzi, K. Vezzù, L. Toniolo, G. Cavinato, Synthesis, studies and fuel cell performance of "core-shell" electrocatalysts for oxygen reduction reaction based on a PtNix carbon nitride "shell" and a pyrolyzed polyketone nanoball "core", International Journal of Hydrogen Energy, 39 (2014) 2812-2827.

[40] V. Di Noto, M. Vittadello, S.G. Greenbaum, S. Suarez, K. Kano, T. Furukawa, A new class of lithium hybrid gel electrolyte systems, Journal of Physical Chemistry B, 108 (2004) 18832-18844.

[41] V. Di Noto, Zeolitic Inorganic−Organic Polymer Electrolyte Based on Oligo(ethylene glycol) 600 K2PdCl4 and K3Co(CN)6, The Journal of Physical Chemistry B, 104 (2000) 10116-10125.

[42] Y. Lu, Y. Jiang, H. Wu, W. Chen, Nano-PtPd cubes on graphene exhibit enhanced activity and durability in methanol electrooxidation after CO stripping-cleaning, Journal of Physical Chemistry C, 117 (2013) 2926-2938.

[43] V. Di Noto, E. Negro, S. Polizzi, P. Riello, P. Atanassov, Preparation, characterization and single-cell performance of a new class of Pd-carbon nitride electrocatalysts for oxygen reduction reaction in PEMFCs, Applied Catalysis B: Environmental, 111-112 (2012) 185-199.

[44] S. Guo, S. Zhang, S. Sun, Tuning nanoparticle catalysis for the oxygen reduction reaction, Angewandte Chemie - International Edition, 52 (2013) 8526-8544.

[45] L. Dubau, T. Asset, R. Chattot, C. Bonnaud, V. Vanpeene, J. Nelayah, F. Maillard, Tuning the Performance and the Stability of Porous Hollow PtNi/C Nanostructures for the Oxygen Reduction Reaction, ACS Catalysis, 5 (2015) 5333-5341.

[46] M.D. Obradović, A.V. Tripković, S.L. Gojković, Oxidation of carbon monoxide and formic acid on bulk and nanosized Pt–Co alloys, Journal of Solid State Electrochemistry, 16 (2012) 587-595.

[47] M.J. Molaei, A. Ataie, S. Raygan, S.J. Picken, The effect of different carbon reducing agents in synthesizing barium ferrite/magnetite nanocomposites, Materials Chemistry and Physics, 219 (2018) 155-161.

[48] U.A. Paulus, T.J. Schmidt, H.A. Gasteiger, R.J. Behm, Oxygen reduction on a high-surface area Pt/Vulcan carbon catalyst: a thin-film rotating ring-disk electrode study, Journal of Electroanalytical Chemistry, 495 (2001) 134-145.

[49] M. Gattrell, B. MacDougall, Reaction mechanisms of the O_2 reduction/evolution reaction, in: V. Vielstich, A. Lamm, H.A. Gasteiger (Eds.) Handbook of Fuel Cells - Fundamentals, Technology and Applications, John Wiley & Sons, Chichester, 2003, pp. 443-464.

[50] A. Pozio, M. De Francesco, A. Cemmi, F. Cardellini, L. Giorgi, Comparison of high surface Pt/C catalysts by cyclic voltammetry, Journal of Power Sources, 105 (2002) 13-19.

[51] H. Yang, C. Coutanceau, J.-M. Léger, N. Alonso-Vante, ClaudeLamy, Methanol tolerant oxygen reduction on carbon-supported Pt–Ni alloy nanoparticles, Journal of Electroanalytical Chemistry, 576 (2005) 305-313.

[52] J.X. Wang, F.A. Uribe, T.E. Springer, J. Zhang, R.R. Adzic, Intrinsic kinetic equation for oxygen reduction reaction in acidic media: The double Tafel slope and fuel cell applications, Faraday Discussions, 140 (2008) 347-362.

[53] D.B. Sepa, M.V. Vojnovic, L.M. Vracar, A. Damjanovic, Different views regarding the kinetics and mechanisms of oxygen reduction at Pt and Pd electrodes, Electrochimica Acta, 32 (1987) 129-134.

[54] B. Hammer, Y. Morikawa, J.K. Nørskov, CO Chemisorption at Metal Surfaces and Overlayers, Physical Review Letters, 76 (1996) 2141-2144.

[55] T.J. Schmidt, H.A. Gasteiger, Rotating thin-film method for supported catalysts, in: V. Vielstich, A. Lamm, H.A. Gasteiger (Eds.) Handbook of Fuel Cells - Fundamentals, Technology and Applications, John Wiley & Sons, Chichester, 2003, pp. 316-333.

[56] S.S. Kocha, Principles of MEA preparation, in: V. Vielstich, A. Lamm, H.A. Gasteiger (Eds.) Handbook of Fuel Cells - Fundamentals, Technology and Applications, John Wiley & Sons, Chichester, 2003, pp. 538-565.

[57] S. Kaytakoğlu, L. Akyalçın, Optimization of parametric performance of a PEMFC, International Journal of Hydrogen Energy, 32 (2007) 4418-4423.

[58] S. Shen, X. Cheng, C. Wang, X. Yan, C. Ke, J. Yin, J. Zhang, Exploration of significant influences of the operating conditions on the local O_2 transport in proton exchange membrane fuel cells (PEMFCs), Physical Chemistry Chemical Physics, 19 (2017) 26221-26229.

[59] F.A. Cotton, G. Wilkinson, C.A. Murillo, M. Bochmann, Advanced Inorganic Chemistry, John Wiley And Sons, New York, 1999.

[60] P.J. Kulesza, J.K. Zak, I.A. Rutkowska, B. Dembinska, S. Zoladek, K. Miecznikowski, E. Negro, V. Di Noto, P. Zelenay, Elucidation of role of graphene in catalytic designs for electroreduction of oxygen, Current Opinion in Electrochemistry, 9 (2018) 257-264.

[61] J. Zak, E. Negro, I.A. Rutkowska, B. Dembinska, V. Di Noto, P.J. Kulesza, Graphene-Based Nanostructures in Electrocatalytic Oxygen Reduction, in: K. Wadelt (Ed.) Encyclopedia of Interfacial Chemistry: Surface Science and Electrochemistry, Elsevier, Amsterdam, 2018, pp. 651-659.

Tables

Table 1. Chemical composition of ECs.

Electrocatalyst	Atomic weight%						Formula
	Pt[a]	Co[a]	K[a]	C[b]	N[b]	H[b]	
PtCo-CN$_l$ 500/C$_{1/4}$	7.48	2.26	0.44	82.2	0.76	0.29	$K_{0.3}[PtCoC_{178}N_{1.4}H_{7.5}]$
PtCo-CN$_l$ 600/C$_{1/4}$	7.76	2.33	0.50	81.2	0.83	0.25	$K_{0.32}[PtCo_{0.99}C_{170}N_{1.5}H_{6.2}]$
PtCo-CN$_l$ 700/C$_{1/4}$	7.63	2.16	1.05	80.6	0.75	0.27	$K_{0.69}[PtCo_{0.94}C_{172}N_{1.4}H_{6.9}]$
PtCo-CN$_l$ 900/C$_{1/4}$	9.27	2.63	0.58	84.4	0.52	0.20	$K_{0.31}[PtCo_{0.94}C_{148}N_{0.8}H_{4.2}]$
PtCo-CN$_l$ 600/C$_{2/4}$	6.84	1.97	0.53	72.6	1.10	0.40	$K_{0.39}[PtCo_{0.95}C_{172}N_{2.2}H_{11.3}]$
PtCo-CN$_l$ 600/C$_{4/4}$	8.56	2.55	0.63	76.6	1.10	0.60	$K_{0.36}[PtCo_{0.99}C_{145}N_{1.7}H_{12.7}]$

[a] By ICP-AES.
[b] By elemental analysis.

Table 2. Parameters describing the ORR performance determined by CV-TF-RRDE measurements.

Electrocatalyst	ECSA / $m^2 \cdot g_{Pt}^{-1}$	$i_{m(0.9\ V)}$ / $A \cdot mg_{Pt}^{-1}$	$i_{s(0.9\ V)}$ / $\mu A \cdot cm_{Pt}^{-2}$
PtCo-CN$_l$ 500/C$_{1/4}$	17.4	0.151	869
PtCo-CN$_l$ 600/C$_{1/4}$	10.3	0.132	1280
PtCo-CN$_l$ 700/C$_{1/4}$	15.3	0.106	692
PtCo-CN$_l$ 900/C$_{1/4}$	4.6	0.030	664
PtCo-CN$_l$ 600/C$_{2/4}$	28.1	0.274	975
PtCo-CN$_l$ 600/C$_{4/4}$	25.6	0.304	1188
Pt/C reference	80.3	0.161	204

Table 3. Performance in PEMFC of ECs. Empirical parameters for the determination of mass transport phenomena in cathodic electrocatalytic layers in the high-current regime.

Cathode electrocatalyst	Maximum Mass Power / W·g_{Pt}^{-1}				$\Psi_{O4/A4}$[c]	$\Psi_{O1/A1}$[d]	$\Psi_{O4/O1}$[e]	$\Psi_{A4/A1}$[f]	Ψ_{av}[g]
	BP[a] = 4 bar		BP[a] = 1 bar						
	O_2[b]	Air[b]	O_2[b]	Air[b]					
PtCo-CN$_l$ 500/C$_{1/4}$	2349	877	736	266	2.68	2.77	3.19	3.30	2.98
PtCo-CN$_l$ 600/C$_{1/4}$	2360	683	707	356	3.46	1.99	3.34	1.92	2.67
PtCo-CN$_l$ 700/C$_{1/4}$	2084	1108	782	593	1.88	1.32	2.66	1.87	1.93
PtCo-CN$_l$ 900/C$_{1/4}$	1864	696	421	258	2.68	1.63	4.43	2.70	2.86
PtCo-CN$_l$ 600/C$_{2/4}$	2481	1066	892	455	2.33	1.96	2.78	2.34	2.35
PtCo-CN$_l$ 600/C$_{4/4}$	2208	820	1002	274	2.69	3.66	2.20	2.99	2.89
Pt/C reference	2325	1901	1405	1143	1.22	1.23	1.65	1.66	1.44

[a] BP = Back Pressure.

[b] Cathode feed.

[c] $\Psi_{O4/A4}$ = Maximum mass power [O_2, 4 bar]/Maximum mass power [Air, 4 bar]

[d] $\Psi_{O1/A1}$ = Maximum mass power [O_2, 1 bar]/Maximum mass power [Air, 1 bar]

[e] $\Psi_{O4/O1}$ = Maximum mass power [O_2, 4 bar]/Maximum mass power [O_2, 1 bar]

[f] $\Psi_{A4/A1}$ = Maximum mass power [Air, 4 bar]/Maximum mass power [Air, 1 bar]

[g] $\Psi_{av} = (\Psi_{O4/A4} + \Psi_{O1/A1} + \Psi_{O4/O1} + \Psi_{A4/A1})/4$

The polarization curves used to evaluate $\Psi_{O4/A4}$, $\Psi_{O1/A1}$, $\Psi_{O4/O1}$ and $\Psi_{A4/A1}$ are reported in Fig. 7, Fig. 8 and in Fig. ESI2 and Fig. ESI3 in the Electronic Supplementary Information.

Table 4. Figures of merit for the performance of ECs in PEMFC tests and mass transport phenomena in cathode electrocatalytic layers in the low-current regime.

Cathode electrocatalyst	V@50 A·g_{Pt}^{-1} / mV				$\Delta_{O4/A4}$[c]	$\Delta_{O1/A1}$[d]	$\Delta_{O4/O1}$[e]	$\Delta_{A4/A1}$[f]	Δ_{av}[g]
	BP[a] = 4 bar		BP[a] = 1 bar						
	O_2[b]	Air[b]	O_2[b]	Air[b]					
PtCo-CN$_l$ 500/C$_{1/4}$	893	797	773	692	96	81	120	105	101
PtCo-CN$_l$ 600/C$_{1/4}$	878	791	787	718	87	69	91	73	80
PtCo-CN$_l$ 700/C$_{1/4}$	890	832	799	777	58	22	91	55	57
PtCo-CN$_l$ 900/C$_{1/4}$	866	783	722	678	83	44	144	105	94
PtCo-CN$_l$ 600/C$_{2/4}$	908	802	785	747	106	38	123	55	81
PtCo-CN$_l$ 600/C$_{4/4}$	868	796	791	705	72	86	77	91	82
Pt/C reference	884	823	827	802	61	25	57	21	41

[a] BP = Back Pressure.
[b] Cathode feed.
[c] $\Delta_{O4/A4}$ = V@50 A·g_{Pt}^{-1} [O_2, 4 bar] – V@50 A·g_{Pt}^{-1} [Air, 4 bar]
[d] $\Delta_{O1/A1}$ = V@50 A·g_{Pt}^{-1} [O_2, 1 bar] – V@50 A·g_{Pt}^{-1} [Air, 1 bar]
[e] $\Delta_{O4/O1}$ = V@50 A·g_{Pt}^{-1} [O_2, 4 bar] – V@50 A·g_{Pt}^{-1} [O_2, 1 bar]
[f] $\Delta_{A4/A1}$ = V@50 A·g_{Pt}^{-1} [Air, 4 bar] – V@50 A·g_{Pt}^{-1} [Air, 1 bar]
[g] Δ_{av} = ($\Delta_{O4/A4}$ + $\Delta_{O4/A4}$ + $\Delta_{O4/A4}$ + $\Delta_{O4/A4}$)/4

Figures

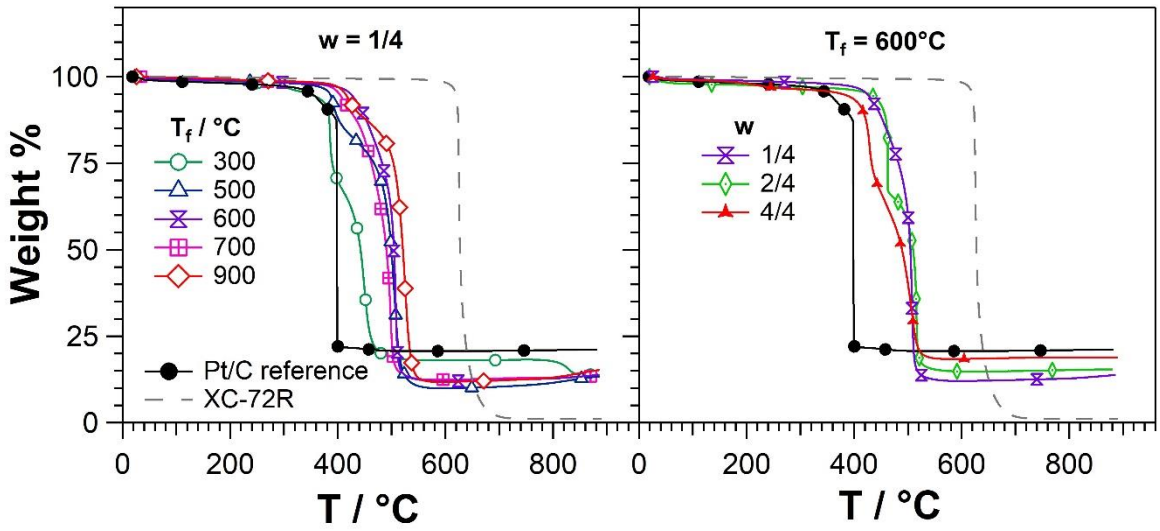

Fig. 1. High-resolution TGA profiles under an air oxidizing atmosphere of the PtCo-CN$_l$ T_f/$C_{1/4}$ (left panel) and PtCo-CN$_l$ 600/C_w (right panel) ECs. High-resolution TGA profiles determined in the same conditions of the Pt/C reference and of the XC-72R carbon black are also introduced in the graphs for the sake of comparison.

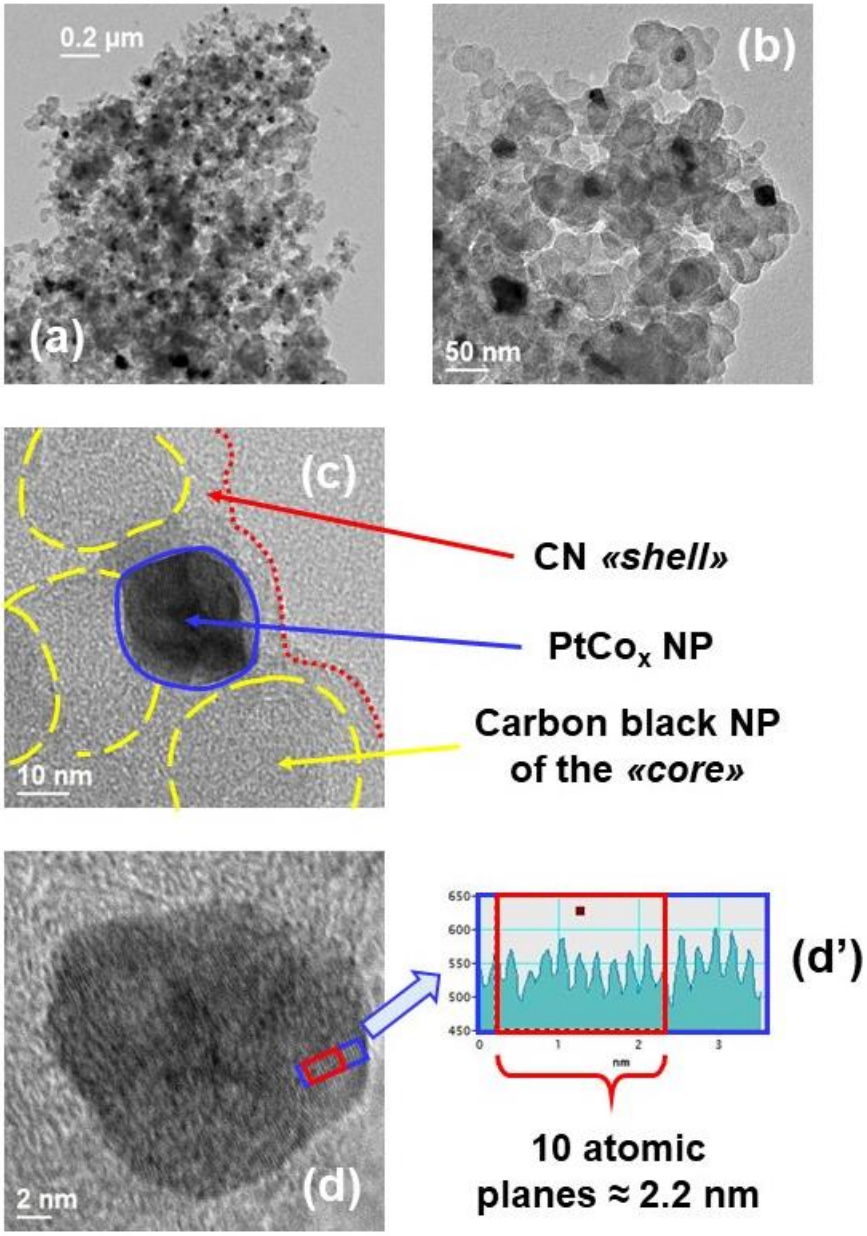

Fig. 2. Morphology of the PtCo-CN$_l$ 600/C$_{2/4}$ EC determined by HR-TEM investigations. Low-magnification micrographs showing the overall features of the EC (a, b); high-magnification micrograph highlighting the *"core-shell"* morphology (c); high-magnification micrograph displaying the morphology and the interplanar fringes of a PtCo$_x$ NP (d); evaluation of the (111) interplanar distance (d').

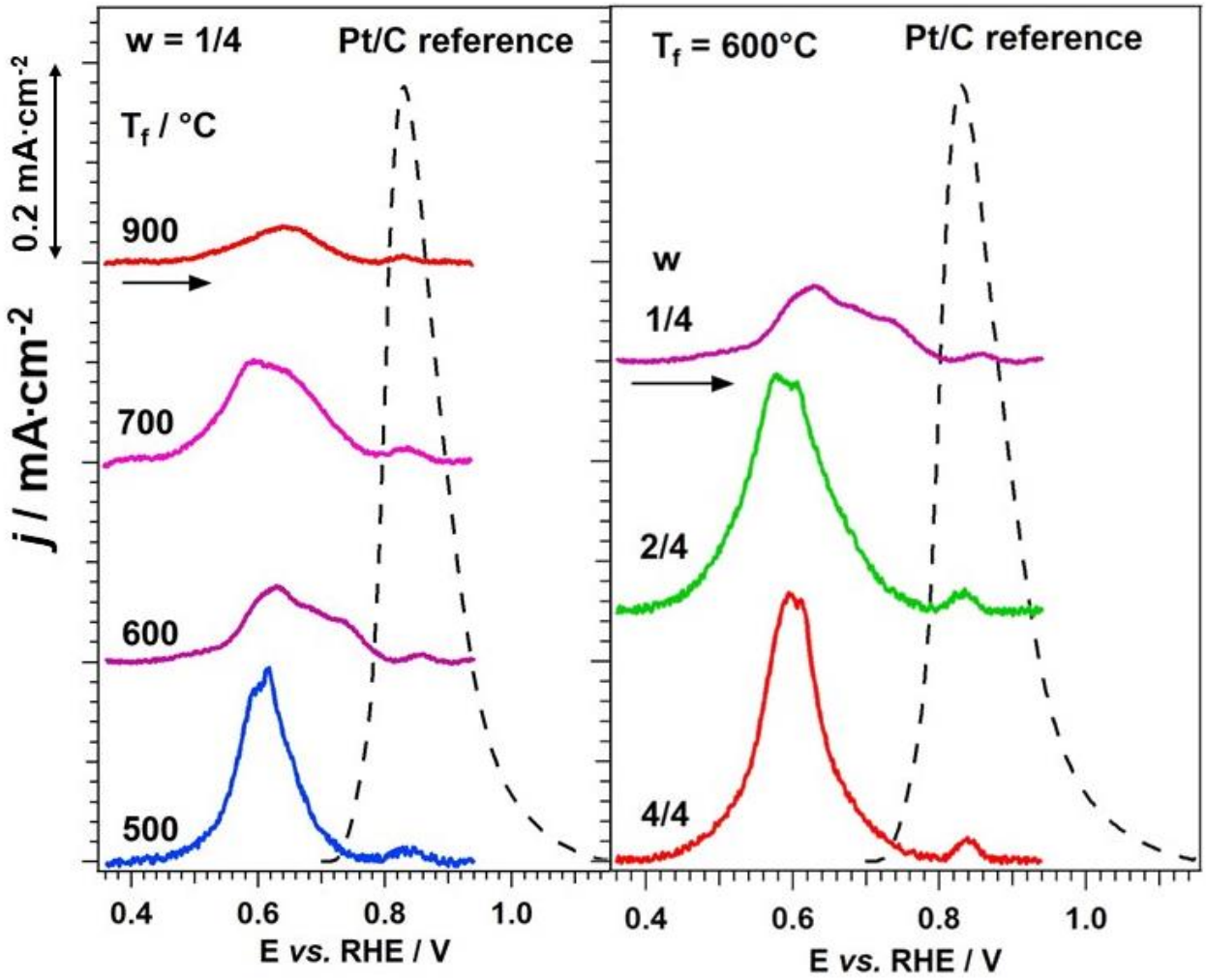

Fig. 3. CO_{ad} stripping current densities of the PtCo-CN_l T_f/C_w ECs. Results obtained on the PtCo-CN_l $T_f/C_{1/4}$ ECs (left panel) and on the PtCo-CN_l 600/C_w ECs (right panel). All the electrodes have a Pt loading of 12 μg·cm^{-2}. A 0.1 M $HClO_4$ solution fills the electrochemical cell, that is thermostated at 25 °C; the sweep rate is 20 mV·sec^{-1}. The electrode tip is not rotated as CO_{ad} is stripped. P_{N_2} = 1 atm; the other experimental details are described in the literature [37].

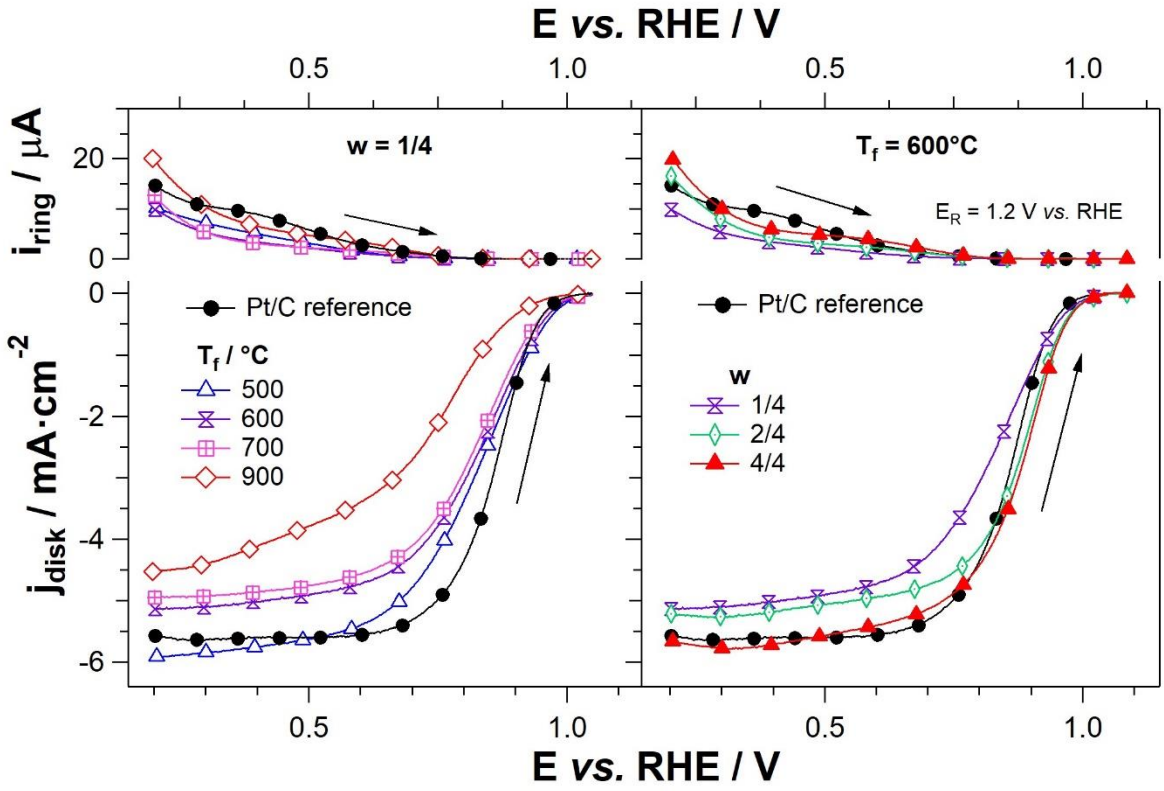

Fig. 4. CV-TF-RRDE profiles of the PtCo-CN$_l$ T_f/C_w ECs in the ORR. Results obtained on the PtCo-CN$_l$ T_f /$C_{1/4}$ ECs (left panel) and on the PtCo-CN$_l$ 600/C_w ECs (right panel). The upper traces are the oxidation currents determined on the Pt ring of the RRDE (i_{ring}). The lower traces are the ORR current densities measured on the glassy carbon disk of the tip (j_{disk}). P_{O_2} = 1 atm; the RRDE is rotated at 1600 rpm. Additional information on the electrodes and on the other experimental conditions is reported in the caption of Fig. 3.

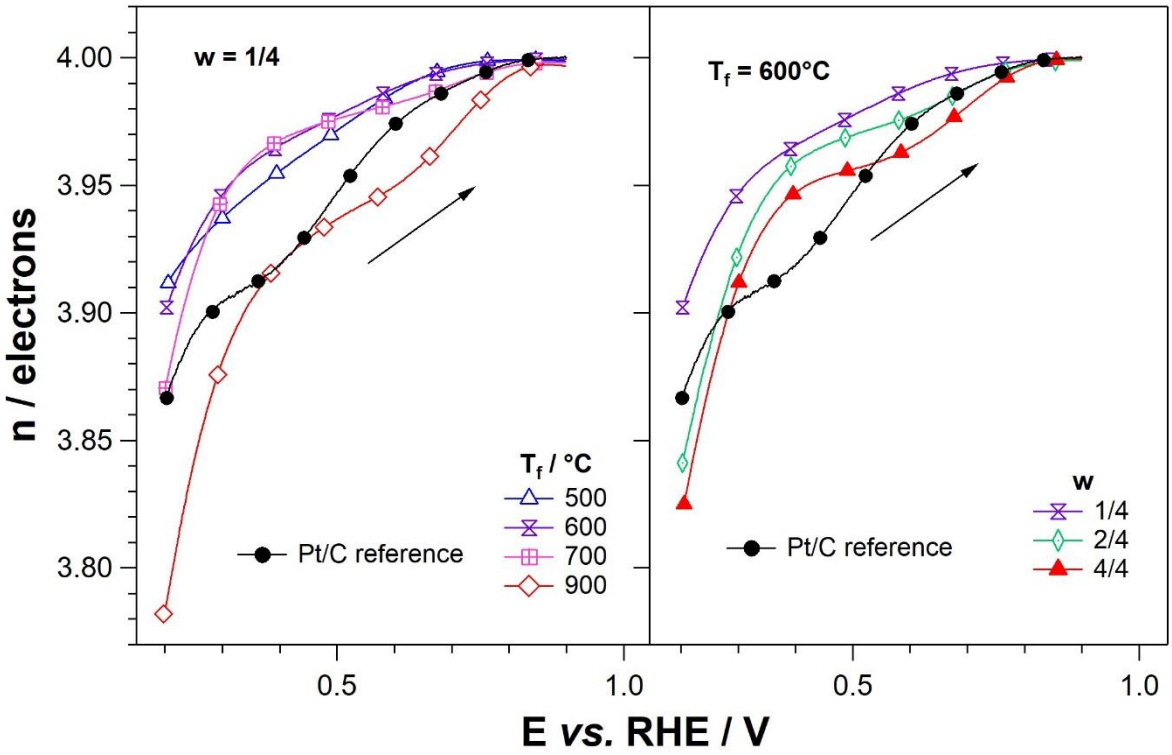

Fig. 5. Average number of electrons (n) that are exchanged during the ORR. Results obtained by means of Equation (1) for the PtCo-CN_l T_f /$C_{1/4}$ ECs (left panel) and for the PtCo-CN_l 600/C_w ECs (right panel) starting from the traces displayed in Fig. 4.

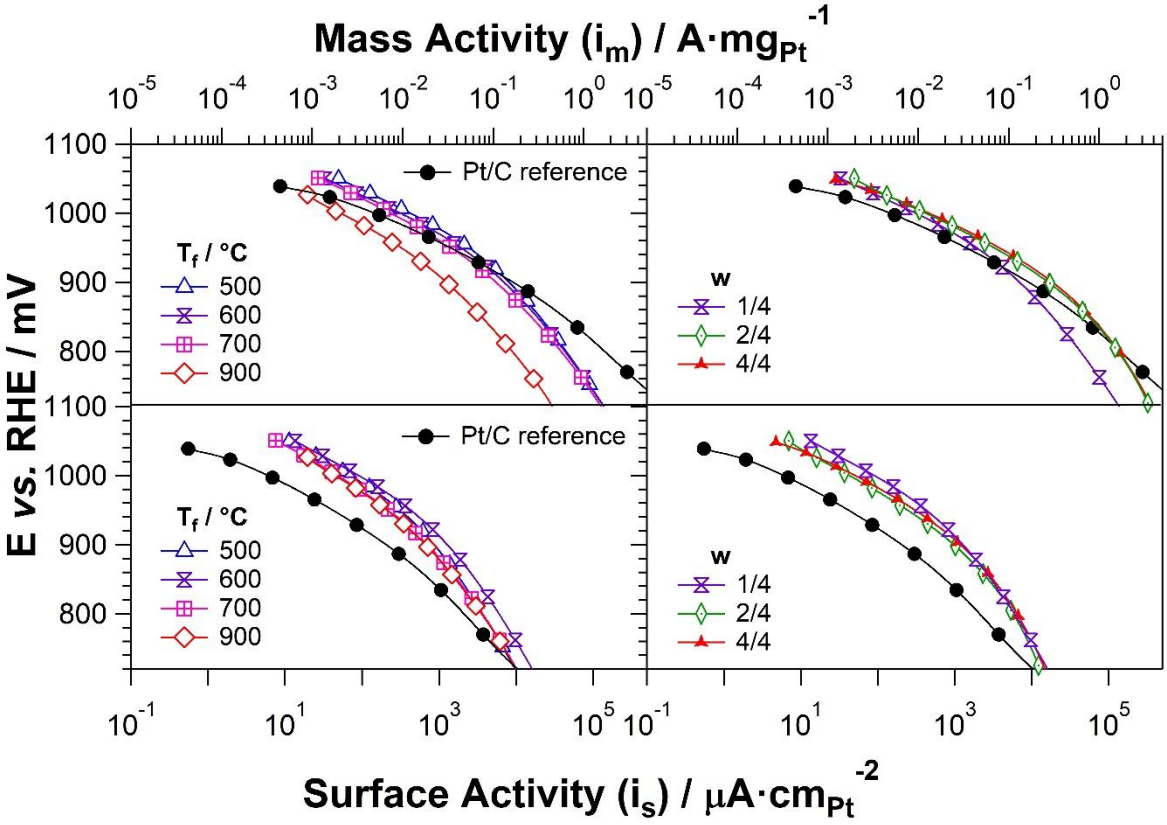

Fig. 6. Tafel plots of the mass activity, i_m (upper panels) and the surface activity, i_s (lower panels) of the PtCo-CN$_l$ T_f/C$_w$ ECs in the ORR. Results refer to the PtCo-CN$_l$ T_f /C$_{1/4}$ ECs (left panels) and to the PtCo-CN$_l$ 600/C$_w$ ECs (right panels). The profiles are determined from the traces displayed in Fig. 4 after removing with Equation (2) the contributions originated by mass transport phenomena.

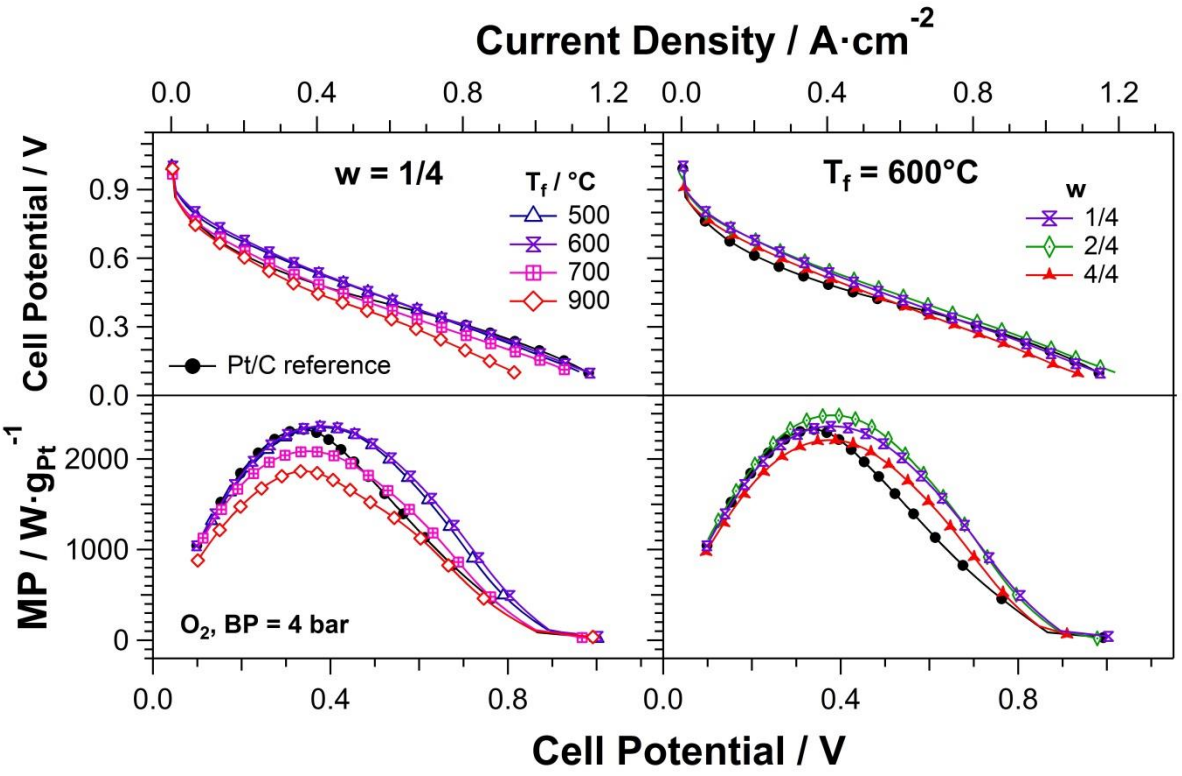

Fig. 7. Results of single fuel cell tests of PtCo-CN$_l$ T_f/C_w ECs mounted at the cathode of a PEMFC. Upper panels: polarization curves. Lower panels: power curves; MP is the *"mass power"*, that is obtained by normalizing the output power yielded by the PEMFC by the mass of Pt on the cathode electrode. Left panels: results determined on PtCo-CN$_l$ $T_f/C_{1/4}$ ECs; right panels: results obtained on PtCo-CN$_l$ 600/C_w ECs. The loading of Pt on the cathode electrode is 0.1 mg·cm^{-2}. The curves are collected on a single-cell PEMFC with a surface area of 5 cm^2 fuelled with pure H_2 on the anode and pure O_2 at the cathode. The flow rates of H_2 and O_2 are 800 and 500 sccm, respectively; $T_{anode/cell/cathode}$ = 84/85/84 °C; the reactants are fully humidified and their back pressure is 4 bar.

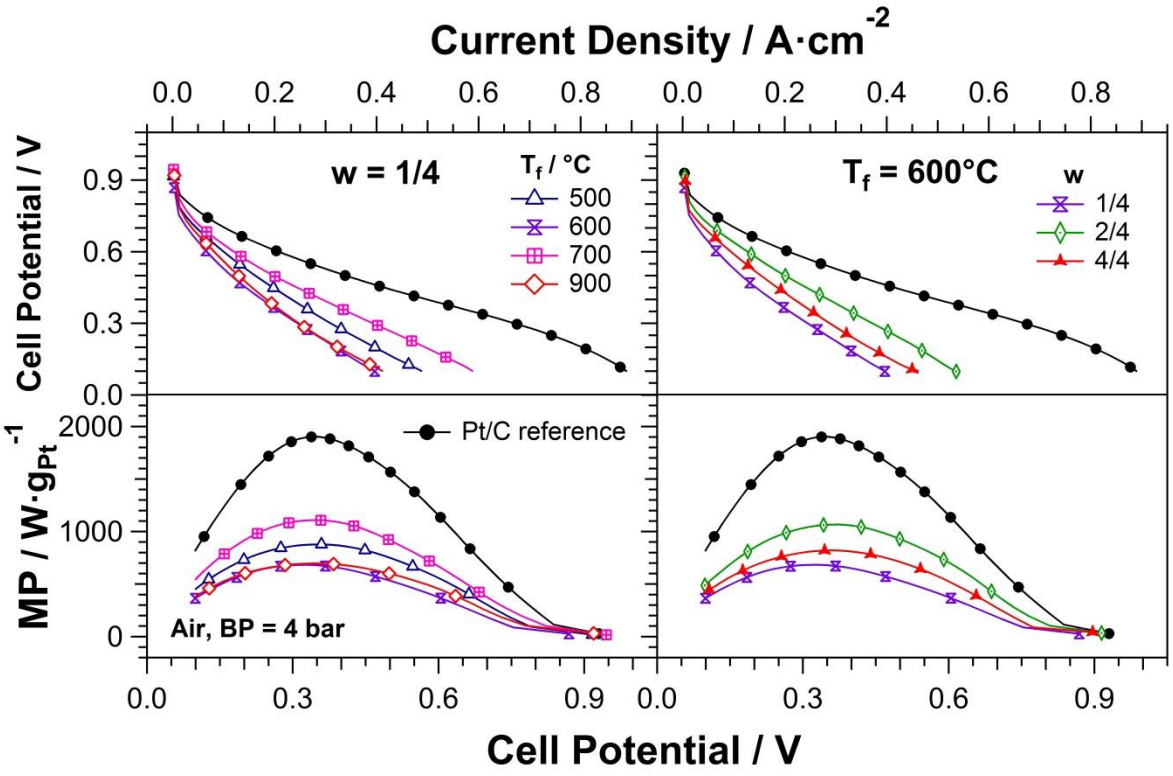

Fig. 8. Results of single fuel cell tests of PtCo-CN$_l$ T_f/C_w ECs mounted at the cathode of a PEMFC. Upper panels: polarization curves. Lower panels: power curves; MP is the *"mass power"*, that is obtained by normalizing the output power yielded by the PEMFC by the mass of Pt on the cathode electrode. Left panels: results determined on PtCo-CN$_l$ $T_f/C_{1/4}$ ECs; right panels: results obtained on PtCo-CN$_l$ 600/C_w ECs. The curves are collected on a single-cell PEMFC with a surface area of 5 cm^2 fuelled with pure H_2 on the anode and air at the cathode. The flow rates of H_2 and air are 800 and 1700 sccm, respectively. The other test conditions are the same as those described in the caption of Fig. 7.

Graphical Abstract

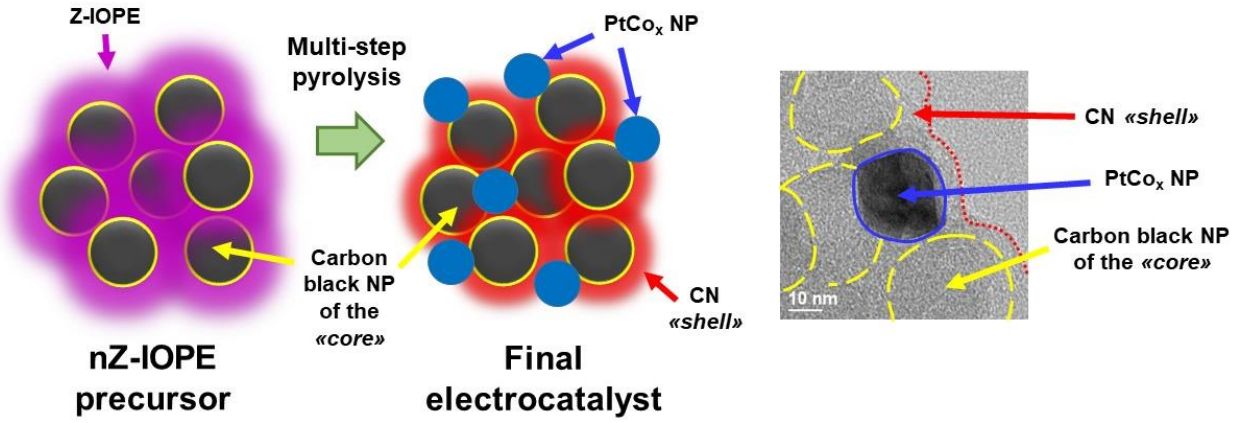

Electronic Supplementary Information for

Correlation between Precursor Properties and Performance in the Oxygen Reduction Reaction of Pt and Co *"Core-shell"* Carbon Nitride-based Electrocatalysts

Vito Di Noto[1,2*], Enrico Negro[1,3], Angeloclaudio Nale[1], Pawel J. Kulesza[4], Iwona A. Rutkowska[4], Keti Vezzù[1,2], Gioele Pagot[1,3].

[1] Section of Chemistry for the Technology (ChemTech), Department of Industrial Engineering, University of Padova, Via Marzolo 9, I-35131 Padova (PD), Italy.

[2] Consorzio Interuniversitario Nazionale per la Scienza e Tecnologia dei Materiali - INSTM, Via Marzolo 1, I-35131 Padova (PD), Italy

[3] Centro Studi di Economia e Tecnica dell'Energia *"Giorgio Levi Cases"*, Via Marzolo 9, I-35131 Padova (PD), Italy.

[4] Faculty of Chemistry, University of Warsaw, Pasteura 1, PL-02-093 Warsaw, Poland

*Corresponding Author. E-mail address: vito.dinoto@unipd.it

S.1. Instruments and methods - WAXD

Wide-angle X-ray diffraction (WAXD) profiles are collected by means of a GNR diffractometer (model eXplorer) mounting a monochromatized CuK$_\alpha$ source; the instrument angle is calibrated using a NIST Si 640d standard. WAXD patters are acquired in the 2θ range 8–90° with a 0.05° step and an integration time of 15 sec. The WAXD patterns of all the PtCo-CN$_l$ T$_f$/C$_W$ ECs are reported in Fig. ESI1 together with the Pt/C reference.

S.2. WAXD profiles

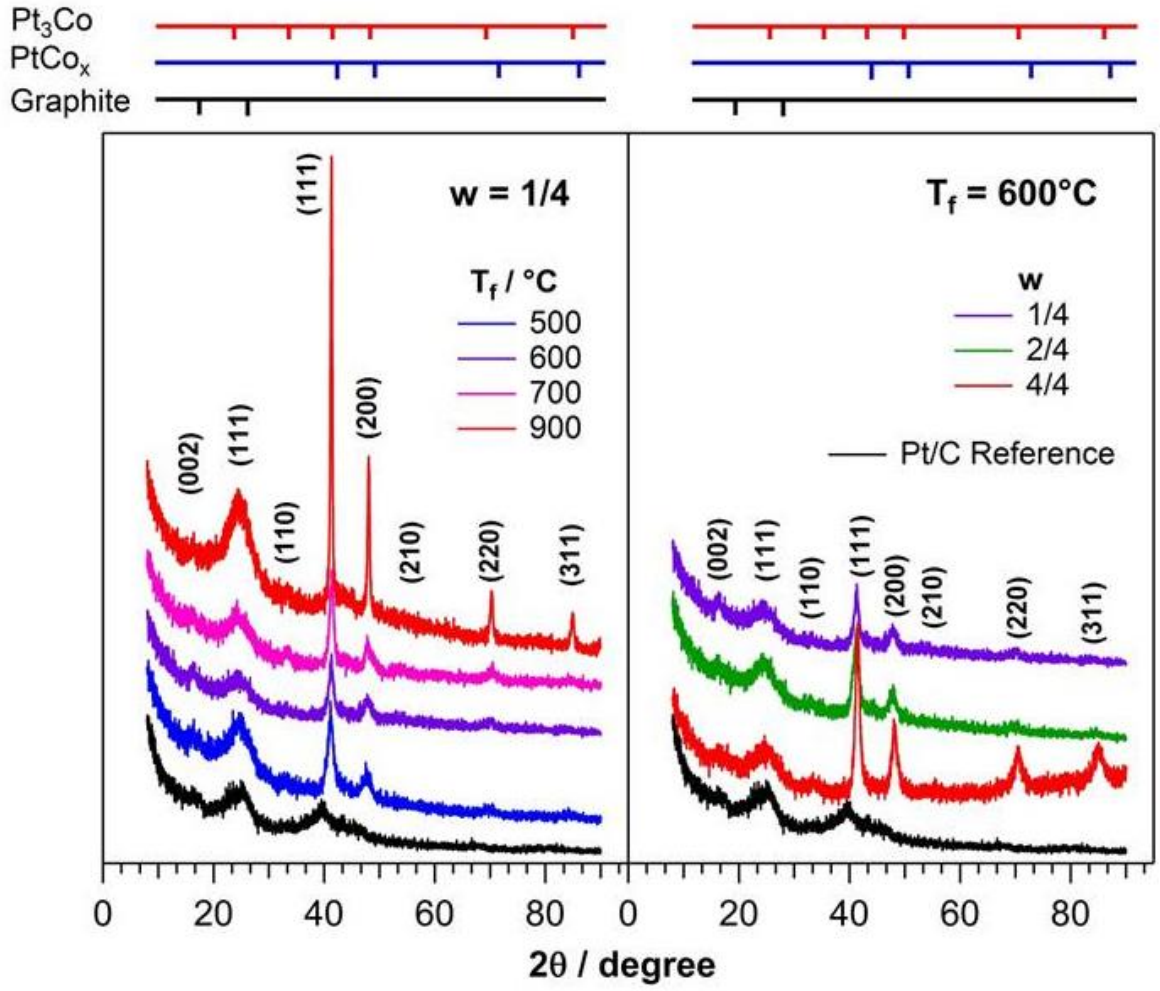

Fig. ESI1. WAXD profiles of PtCo-CN$_l$ T$_f$/C$_{1/4}$ (a) and PtCo-CN$_l$ 600/C$_w$ (b).

Two groups of peaks are detected: (i) sharp peaks at 2θ ~ 41° (111), 48° (200), 70° (220) and 84° (311) are reflections of alloy NPs with an fcc structure and belonging to the Fm3m space group, which correspond to $PtCo_x$ phases; and (ii) broader peaks at 2θ ~16° and 25° ascribed to the contribution of both the graphitic CN *"shell"* and the XC-72R NPs of the support *"core"*. In addition, at $T_f \geq 600$ °C a very small amount of an ordered Pt_3Co crystal phase is detected by weak reflections at 2θ ~ 33° (110) and 53.1° (210). Pt_3Co belongs to the space group Pm3m. Typical reflections of crystalline Pt and Co are not observed. The particle size of the $PtCo_x$ phase is determined by the Scherrer's method. The results are reported in Table ESI1.

Table ESI1. Particle size of the $PtCo_x$ phase as determined by the Scherrer's method.

Electrocatalyst	Particle size / nm
PtCo-CN$_l$ 500/C$_{1/4}$	7.9
PtCo-CN$_l$ 600/C$_{1/4}$	9.5
PtCo-CN$_l$ 700/C$_{1/4}$	12.8
PtCo-CN$_l$ 900/C$_{1/4}$	30.3
PtCo-CN$_l$ 600/C$_{2/4}$	10.3
PtCo-CN$_l$ 600/C$_{4/4}$	11.1
Pt/C reference	2.8[(a)]

[(a)] This phase only includes Pt.

S.3. Polarization and power curves

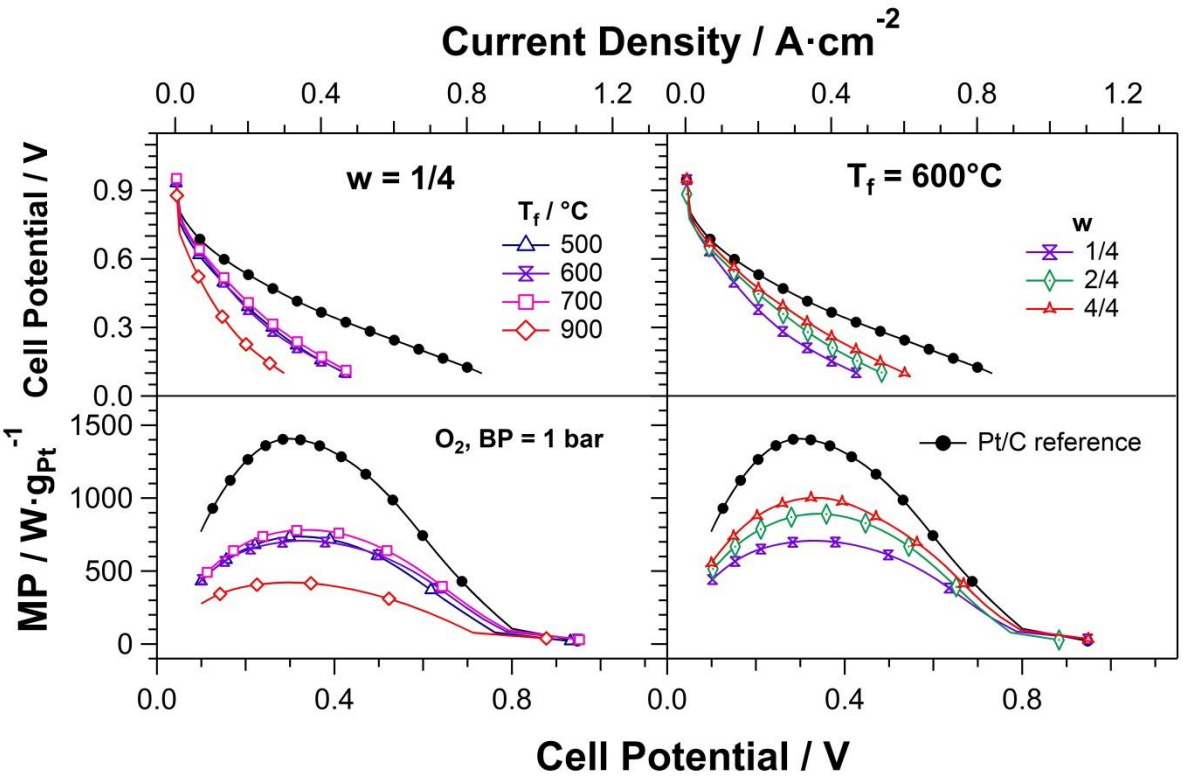

Fig. ESI2. Results of single fuel cell tests of PtCo-CN$_l$ T_f/C_w ECs mounted at the cathode of a PEMFC. Upper panels: polarization curves. Lower panels: power curves; MP is the *"mass power"*, that is obtained by normalizing the output power yielded by the PEMFC by the mass of Pt on the cathode electrode. Left panels: results determined on PtCo-CN$_l$ T_f/$C_{1/4}$ ECs; right panels: results obtained on PtCo-CN$_l$ 600/C_w ECs. The loading of Pt on the cathode electrode is 0.1 mg·cm^{-2}. The curves are collected on a single-cell PEMFC with a surface area of 5 cm^2 fuelled with pure H_2 on the anode and pure O_2 at the cathode. The flow rates of H_2 and O_2 are 800 and 500 sccm, respectively; $T_{anode/cell/cathode}$ = 84/85/84 °C; the reactants are fully humidified and their back pressure is 1 bar.

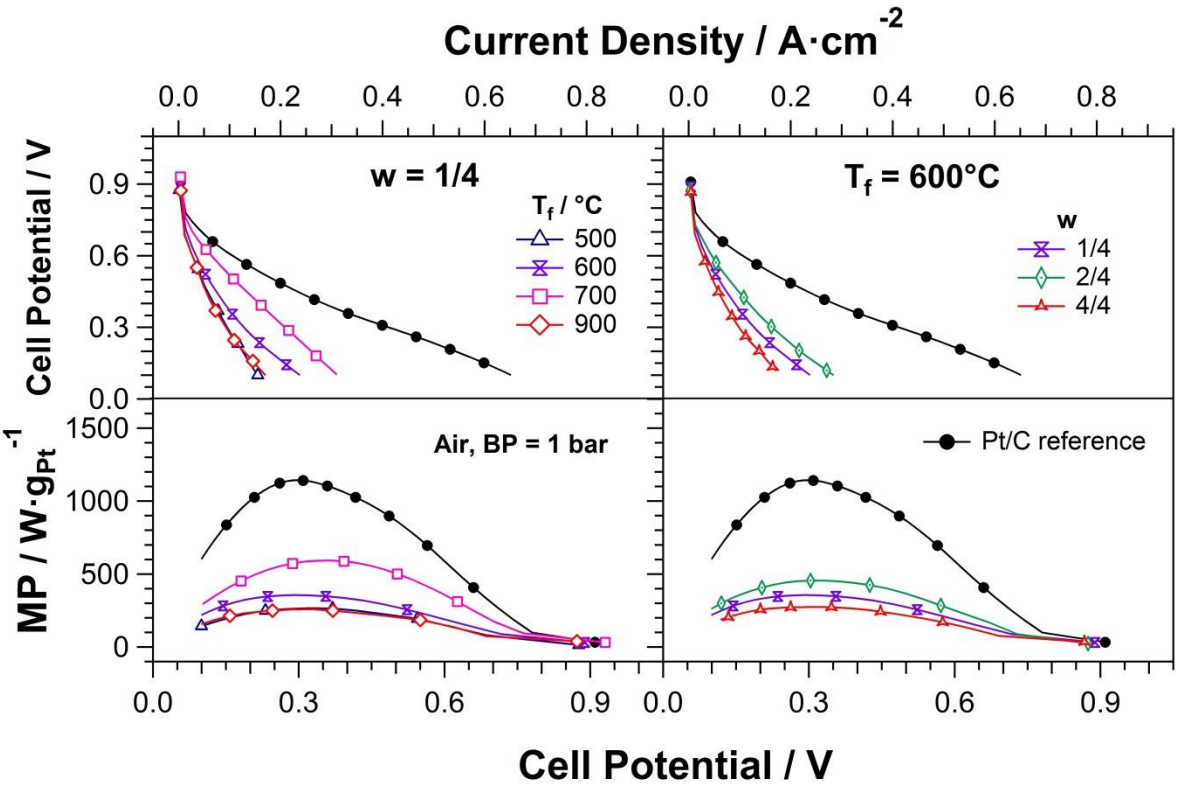

Fig. ESI3. Results of single fuel cell tests of PtCo-CN$_l$ T_f/C_w ECs mounted at the cathode of a PEMFC. Upper panels: polarization curves. Lower panels: power curves; MP is the *"mass power"*, that is obtained by normalizing the output power yielded by the PEMFC by the mass of Pt on the cathode electrode. Left panels: results determined on PtCo-CN$_l$ $T_f/C_{1/4}$ ECs; right panels: results obtained on PtCo-CN$_l$ 600/C_w ECs. The loading of Pt on the cathode electrode is 0.1 mg·cm^{-2}. The curves are collected on a single-cell PEMFC with a surface area of 5 cm^2 fuelled with pure H_2 on the anode and air at the cathode. The flow rates of H_2 and air are 800 and 1700 sccm, respectively; $T_{anode/cell/cathode}$ = 84/85/84 °C; the reactants are fully humidified and their back pressure is 1 bar.